# Single-Mode Lasing in Cavities of Different Dimensionalities

*Wanwoo Noh*

Electrical Engineering and Computer Sciences
University of California, Berkeley

Technical Report No. UCB/EECS-2022-111
http://www2.eecs.berkeley.edu/Pubs/TechRpts/2022/EECS-2022-111.html

May 13, 2022

# Single-Mode Lasing in Cavities of Different Dimensionalities

By

Wanwoo Noh

A dissertation submitted in partial satisfaction of the
requirements for the degree of
Doctor of Philosophy
in
Engineering – Electrical Engineering and Computer Sciences
in the
Graduate Division
of the
University of California, Berkeley

Committee in charge:

Professor Boubacar Kanté, Chair
Professor Eli Yablonovitch
Professor Costas Grigoropoulos

Spring 2022

# Abstract

# Single-mode Lasing in Cavities of Different Dimensionalities

by

Wanwoo Noh

Doctor of Philosophy in Electrical Engineering and Computer Sciences
University of California, Berkeley

Professor Boubacar Kanté, Chair

Semiconductor lasers based on microcavities have attracted a large amount of interest owing to their potential as highly integrated components in photonic circuits as well as diverse applications. Microcavity having a small modal volume is now one of the most essential components in the modern photonics, and its form has been extensively diversified thanks to recent improvements in nanofabrication. However, it has still been challenging for different types of cavities to operate under single mode and to lase in a preselected mode. This dissertation proposed three different techniques used to preselect and maintain single-mode lasing in cavities of different dimensionalities.

Chapter 2 presents zero-dimensional microdisk resonators self-suspended by connecting bridges. The bridges offer mechanical support to suspend microdisks, and more importantly, can be used to enhance or reduce wave confinement in the whispering gallery mode depending on the azimuthal of modes and symmetry of bridge configurations. By tuning the quality factor of modes in microdisks, we have demonstrated single-mode lasing devices that exploit the arbitrary order whispering gallery mode.

Chapter 3 demonstrates single-mode lasing of valley-Hall ring cavities using the interface (1D) between two topologically distinct photonic crystals. We present that the degree of asymmetry governs four photon confinement regimes at the interface of topologically distinct valley-Hall domains, and, controls an interplay between the width of the topological bandgap and the quality factor of ring-like modes for single-mode operation.

Chapter 4 describes a single-mode lasing cavity based on the 2D photonic crystal array. It is shown that a carefully designed photonic crystal based on Dirac point scales infinitely while operating under single mode. Near the singularity, competing higher order modes are efficiently suppressed when the bands are mixed with more lossy ones, and the fundamental mode having a flat envelope makes all unit-cells in the same phase. We also discuss the experimental details on fabrications and characterizations of large-scale photonic crystal arrays.

*To My Family*

# Table of Contents

# Acknowledgments

It is still hard to believe that I will graduate soon. It has been a long but unforgettable journey during my Ph.D. starting from the beginning. It has never been completed if I couldn't get support and guidance from people I would like to sincerely thank here. First, I would like to thank my advisor, Prof. Kanté, for his mentorship and support for six years. I'm very grateful to him for giving me a great opportunity to work with you in the great Californian cities, San Diego and Berkeley. I was lucky to see and learn from him hard-working, scientific thinking, passion as well as initiative. In addition, I also would like to thank Prof. Eli Yablonovith, Prof. Ming Wu, and Prof. Costas Grigoropoulos as well as Prof. Yeshaiahu Fainman, and Prof. Zhaowei Liu at UC San Diego for their priceless and insightful feedback during my preliminary and qualifying exams.

I also must give huge credit to my incredible colleagues in our group, Matthieu, Abdoulaye, Ashok, Babak, LiYi, Junhee, Jeongho, Chi-Hsin, Quynh, Hadiseh, Rushin, Mutasem, Zhetao, Kevin, Hwi-Min, Emma, Yertay, Christos, Walid, and Wayesh. I was lucky to work with the most brilliant people I have ever met, and I couldn't finish this trip without the time we have fun together, discussing, arguing, camping, and betting on hot chocolates for national soccer matches. I wish my best to everyone in their positions, regardless of where and when until we hang out in the future. Additionally, I am grateful to all the staff members in the administration office and cleanroom both at UC Berkeley and UC San Diego, especially Maribel, for helping my experiments for my entire Ph.D.

Lastly and most importantly, many thanks to my family, my Dad, Mom, and sister, who were always there for me and supported me with unconditional love, whenever the time is easygoing or tough. The fact that you are all proud of me was a huge motivation for me to finish the long journey. I feel sorry that I couldn't visit home more often but we'll have more time after graduation. Additionally, I would like to thank Uri, for being with me in one of the toughest times in my life, especially during the pandemic. I'm more than excited to see what waits for us in our future. I also want to thank all my friends, colleagues, and staff I've met during my degree for their help and support.

# 1

# *Introduction*

## 1.1 Semiconductor lasers based on microcavities

Semiconductor lasers have been extensively investigated for their essential role in science and technology as well as widespread applications in several areas including military, health, telecommunication, automotive, and manufacturing, with the advantage of electrical carrier injection and pumping. Thanks to the improvement in lithographic tools including electron beam writers in recent decades, an extremely small-scale top-down patterning, sometimes even smaller than the emission wavelength of the light, has been enabled. Semiconductor lasers having a small footprint and modal volume can be designed and fabricated by using several types of the microcavity. In the early 1980s, the vertical-cavity surface-emitting laser (VCSEL) was one of the pioneering inventions in the field of semiconductor lasers using Bragg reflectors as their facet mirrors of Fabry-Perot cavities. VCSELs are now one of the most successfully commercialized types of semiconductor lasers thanks to their advantages in mass production. Soon after, microdisk lasers using whispering gallery modes have been demonstrated and studied extensively because of their relatively simple fabrication, small footprint, and low threshold. With its ultrahigh quality factor and wave confinement, microdisks have been used as an essential component in a photonic integrated circuit or a sensor as well. After its first proposal in the late 80s, photonic crystal based on the periodical refractive index change extended the dimension of light modulation into two dimensions from simple Bragg mirrors. The experimental demonstration of defect cavity laser based on photonic crystal was aided by the improvement in nanofabrication technique later. Due to their tunability of light using the symmetry of the unit lattice, photonic crystal surface-emitting lasers have been attracting wide interest up until now. In the new millennium, there have been even more endeavors to reduce the size of the cavity just like those in the field of semiconductor electronics. Recently, the metallo-dielectric and plasmonic cavities brought the size of the cavity to even smaller than the emission wavelength and shrunk the optical mode dimension to smaller than the diffraction limit.

## 1.2 Single-mode operation in microcavity lasers

One of the challenges of semiconductor laser operation is to maintain single-mode lasing for a specific mode to utilize high spectral purity, which is a unique advantage of a laser. It becomes harder if the cavity contains a larger number of competing modes within the gain bandwidth of material. When the cavity is designed properly, the target lasing mode usually coincides with the peak of the gain spectrum of material, and lasing occurs when the gain is equal to the loss in the medium. However, in most cases, cavities accompany higher (or different) order modes that compete with the target mode. There are fundamentally two ways to maintain single-mode lasing as illustrated in Fig. 1. Fig.1a describes when more than one mode is competing with the target mode in the middle. In this case, harmful effects are expected for laser operation including undesirable mode competition and subsequent gain saturation as well as mode hopping. The first way to address this issue is to enhance the target mode and/or suppress the competing modes by engineering the loss of modes (Fig.1b). A phase-shift distributed feedback Bragg lasers, VCSELs, and pumping modulations make good examples. The other method is to adjust the mode separation or increase the free spectral range (Fig.1c). A single-cell defect cavity and linear dispersion photonic crystal laser exemplify this case.

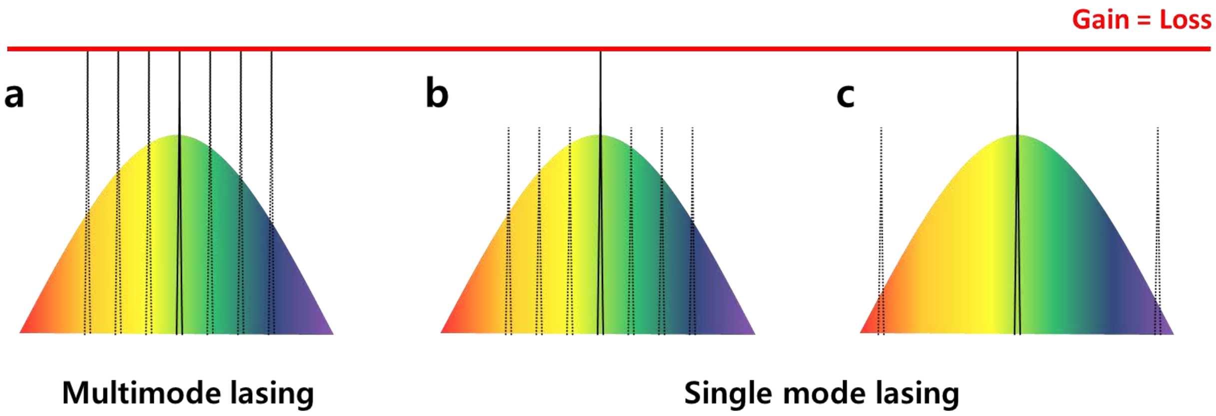

**Fig. 1.** A schematic illustrating multimode cavity and two strategies to maintain single-mode lasing.

In this dissertation, we propose three strategies used to maintain single-mode lasing operations in cavities of different dimensionalities. First, for microdisk lasers having a zero-dimension because of their ultrasmall footprint and mode confinement, we demonstrate the external structure, which are bridges connecting to the disk, can be used to either protect or suppress the specific order of whispering gallery modes. Second, we report a single-mode lasing of the valley-Hall ring cavity that consists of a one-dimensional interfacial waveguide between two inverted photonic crystals, at telecommunication wavelength for the first time in the field. Topology plays a fundamental role in modern physics and enables new information processing techniques and wave device physics with built-in robustness. However, the creation of photonic topological phases usually requires complicated structures that limit the potential for miniaturization and integration. By controlling the degree of asymmetry in a photonic crystal with broken inversion symmetry, single-mode lasing was achieved. Finally, to resolve a long-lasting question of scaling of the single-aperture lasing cavity, we theoretically proposed and experimentally demonstrate an open-Dirac singularity-based two-dimensional photonic crystal surface-emitting laser with infinite scalability. It is worth noting that the first two types of cavities, 0D microdisks and 1D valley-Hall cavity, were optimized for single-mode operation using the first strategy of suppressing undesirable modes, while the 2D photonic crystal cavities were designed to suppress higher-order mode and to increase the free spectral range at the same time. Our results on the optimization of microcavities for single-mode lasing will open the door to novel optoelectronic devices and systems using microcavities in general.

# 2

# *Single-Mode Microdisk Laser*[*]

## 2.1 Introduction

Over the past few years, small-scale lasers have attracted widespread attention with potential applications in several areas including health,[1,2] defense,[3] and quality control,[4] to name a few. Recent advances made in photonics, both in understanding physical phenomena[5,6] and in controlling fabrication processes,[7,8] have contributed to improved laser robustness[9] and size.[10,11] A semiconductor laser having a small modal volume can be designed by implementing various cavities such as Bragg mirror,[12–14] microdisk,[15–21] photonic crystal,[22–25] metallo-dielectric resonator,[26,27] and plasmonic cavity.[28,29] Especially, microdisk lasers using high quality factor whispering gallery mode (WGM) are promising candidates owing to their low threshold, small modal volume, and simplicity of fabrication. The use of WGMs as lasers is of interest because of their small footprint, their high spectral sensitivity, and their potential for on-chip integration.[30] To exploit the properties of WGMs, a microdisk resonator with an underlying post using the undercut etching method has been investigated in many previous studies.[15–21] However, the underlying post used for mechanical support may hamper the intrinsic field profile of WGMs and does not contribute to mode selection.[18]

Another challenge of laser operation is to maintain single-mode lasing for specific modes due to

---

[*] The following section is published in ACS Photonics. (W. Noh, M. Dupré, A. Ndao, A. Kodigala, B. Kanté, “Self-Suspended Microdisk Lasers with Mode Selectivity by Manipulating the Spatial Symmetry of Whispering Gallery Modes”, ACS Photonics, 9, 389-394, 2019)

the high number of closely spaced WGMs. In addition, any WGMs in the azimuthally symmetric cavity fundamentally have two-fold degeneracy,[30] which brings deleterious effects such as undesirable mode competition and consequent gain saturation and mode hopping when imperfection appears in practice.[31] To date, single-mode lasing has been enabled by breaking degeneracy and suppressing undesirable modes by inserting additional features in the resonator such as grating[32], groove[33,] and nanoantenna[34,35], by breaking parity-time symmetry[36,37], or by injecting appropriate optical pulse input.[38]

In this chapter, we present simple microdisk lasers whose cavity consists of a cylindrical resonator and bridges for self-suspension symmetrically placed at every $2\pi/N$ where $N$ is the number of bridges. The freestanding platform provides higher mode confinement compared to suspended microdisks with a post[15–21] due to the improved index contrast between microdisks and the surrounding medium (air). We also find that bridges not only provide mechanical stability but also maintain or reduce the quality factor of WGMs depending on their configuration. Interestingly, the quality factor of WGMs is enhanced when the number of bridges matches the number of antinodes of WGMs. By optimizing the configuration of bridges, we experimentally demonstrate single-mode lasing at telecommunication wavelength for various WGMs.

## 2.2 Mode selection by manipulating spatial symmetry of whispering gallery modes

To understand the mode behavior of microdisk cavities, we first calculated the eigenmode of simple microdisks without any bridges by using the finite element method. COMSOL Multiphysics$^{TM}$ is used for eigenmode simulation. Fig. 1a illustrates a simple microdisk with a thickness of 300 nm, modeled in the numerical simulation using a refractive index of n=3.45 and open boundary conditions. WGMs are commonly labeled using three indices, the radial index (*l*), the azimuthal index (*m*), and the slab index (*p*). *l*-1, *m*, and *p*-1 represent the number of radial, azimuthal, and z-direction nodes, respectively.[40] The normalized electric field and magnetic field distribution of each mode in the middle of the cylinder (z-axis) identifies TE WGMs as shown in Fig. 1b. Fig. 1c and d present respectively the resonant wavelength and quality factor for four TE WGMs as a function of their radius. It is worth noting that TE ($H_z$ dominant) and TM ($E_z$ dominant) WGMs have incomparably higher quality factors than any other Mie mode in the microdisk.[15] As shown in Fig. 2b comparing the quality factor between the TE and TM WGMs, TE modes always have a higher quality factor in a thin disk configuration, and the difference increases as the radius increases.[41] Therefore, we consider only TE WGMs without any radial or slab node (*l*, *p*=1) in our further discussion in terms of lasing mode. In the gain bandwidth of our interest, TE WGMs with *m*=3 to 6 appear and the resonant wavelength of each mode naturally increases as the radius increases (Fig. 1c). In general, for a given radius of the cylinder, WGMs with higher *m* are at a higher frequency. As *m* increases, the quality factor of WGMs also increases because higher order modes couple less efficiently to the far-field. Note that the wavelength range in the calculation from 1100 nm to 1700 nm corresponds to the gain spectrum of InGaAsP MQWs wafers used in the experiment. Fig. 3 plots the spontaneous emission spectrum measured from the bare wafer.

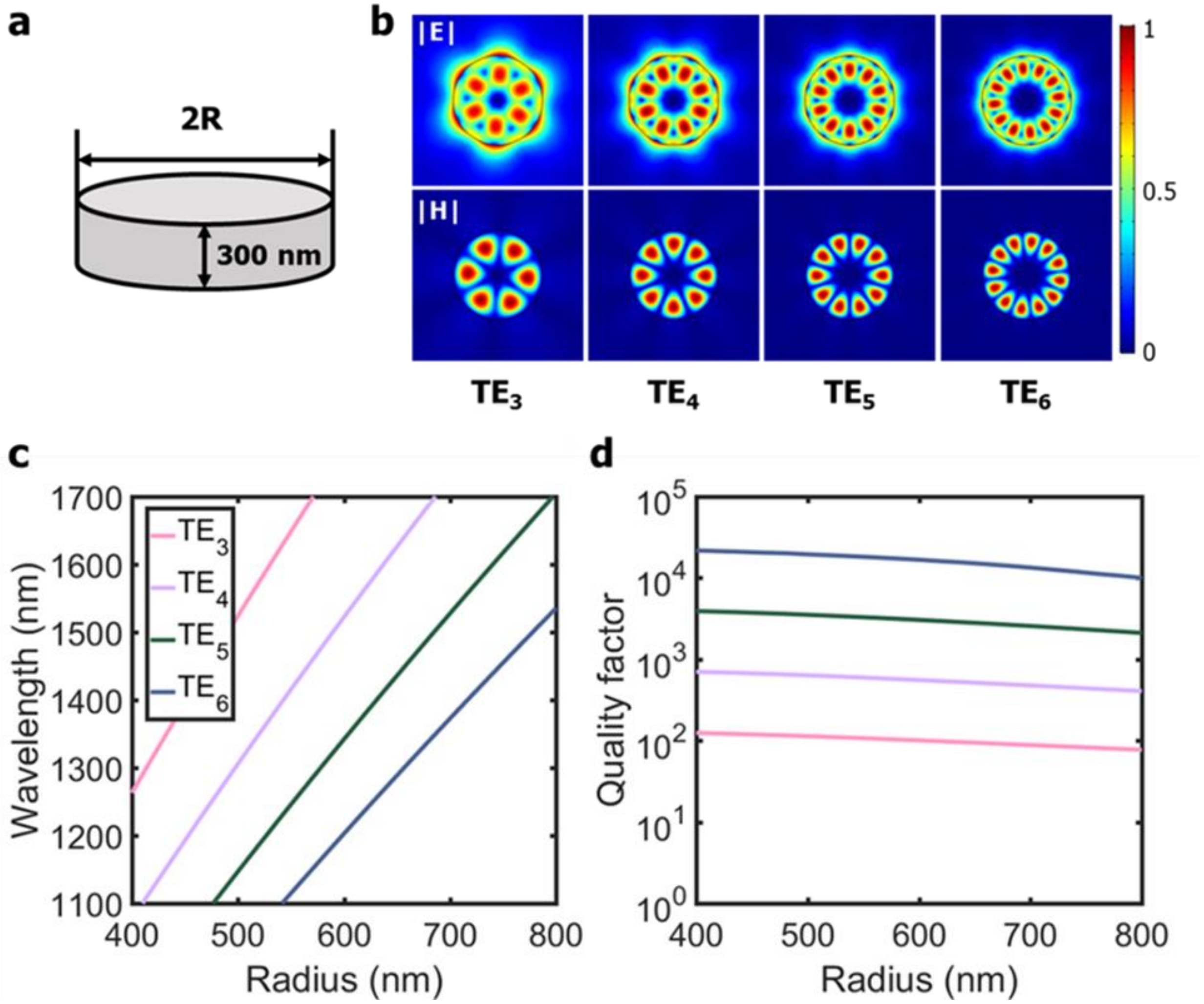

**Fig. 1.** Modes of a cylindrical dielectric resonator. **a**, Cylinder resonator with characteristic dimensions. **b**, Normalized distribution of electric and magnetic field magnitude of WGMs with azimuthal index m=3 to 6. **c**, Resonant wavelength and **d**, quality factor of four WGMs as a function of the radius of the cylinder.

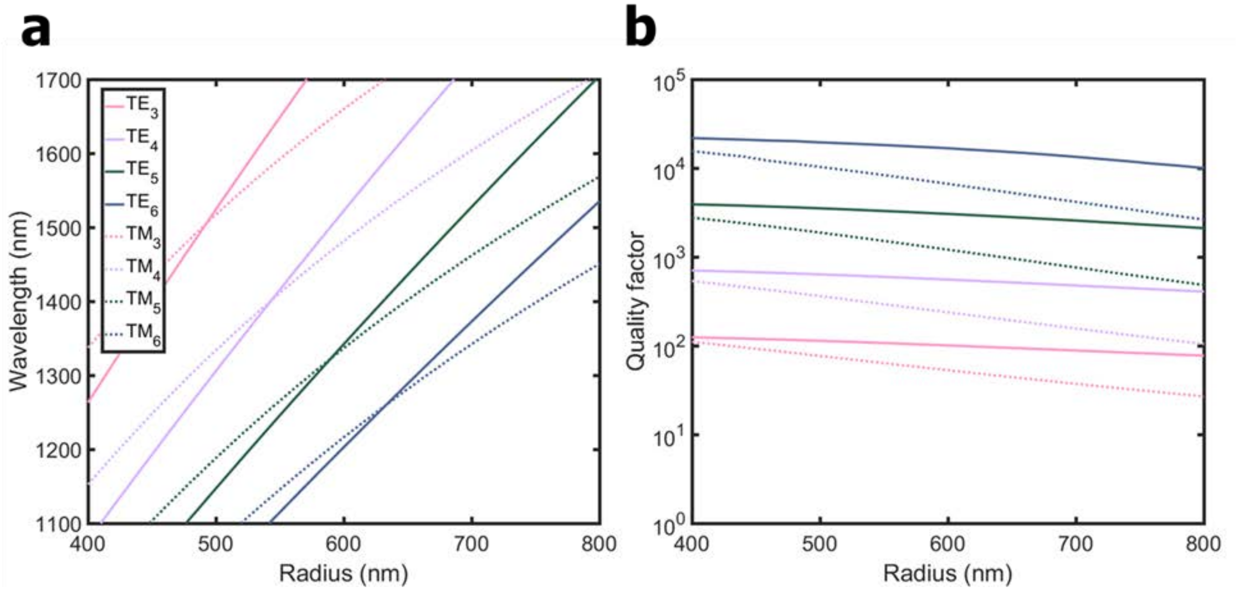

**Fig. 2**. **a**, Resonant wavelength and **b**, quality factor of TE (solid lines) and TM (dotted lines) WGMs with *m* from 3 to 6 as a function of the radius of the cylinder. TE WGMs always have higher quality factor than TM WGMs with same azimuthal index *m*.

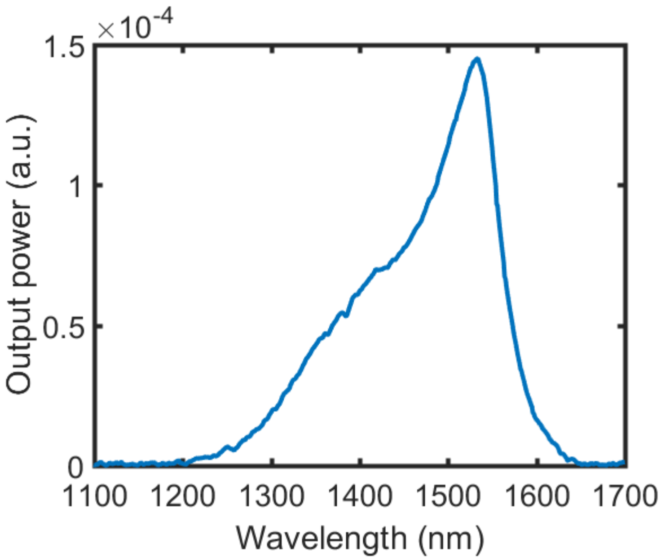

**Fig. 3.** Spontaneous emission spectrum measured from the bare InGaAsP MQWs wafer, showing gain bandwidth from 1100 to 1700 nm. Gain is highest around 1550 nm.

We now investigate the effect of bridges. They play an important role in both the self-suspension of the cavity and the selection of the WGMs. In the simple cylindrical configuration without bridges, as illustrated in Fig. 1b, the WGMs have three notable characteristics in terms of field distribution. First, the mode is mainly confined around the perimeter of a cylinder. Second, the field pattern has $2m$-fold rotational symmetry. For instance, the $TE_4$ ($l$=1, $m$=4, $p$=1) mode has 8-fold rotational symmetry. Finally, the WGMs intrinsically have two-fold degeneracy, and thus two eigenmodes degenerate with the same frequency and quality factor. Fig. 4 shows that this degeneracy can selectively be lifted or not depending on bridge configuration with the example of $TE_4$ mode. Fig 4a shows the two calculated degenerate modes which are identical in both resonant wavelength and quality factor. When the bridges maintain the spatial symmetry of the WGM or the number of bridges $N$ is the divisor of the total number of antinodes of mode, the doubly degenerate $TE_4$ mode is split into two modes due to the spatial perturbation. This case corresponds to Fig. 4b. When the number of bridges is two, one of the modes is maintained with the almost same field profile with a similar or slightly increased quality factor (Fig. 4b, left), but the other mode does not keep the same field profile and its quality factor is significantly decreased (Fig. 4b, right). The lower quality factor mode can be disregarded in considering lasing mode as it will not favorably compete for gain. On the other hand, if the number of bridges $N$ breaks the 8-fold symmetry of the $TE_4$ mode pattern, or $N$ is not the divisor of the total number of antinodes of mode, the degeneracy is not lifted and two eigenmodes are maintained. Fig 4c presents this case with the three bridges. In this case, however, the quality factor of modes also decreases due to the mismatch, and it is not preferred for lasing mode selection as well.

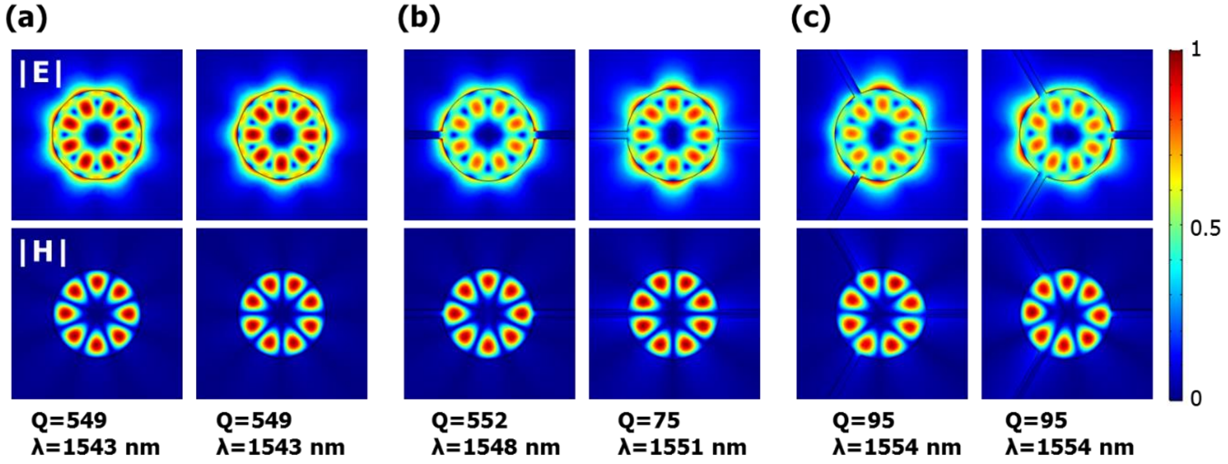

**Fig. 4.** Normalized distribution of electric and magnetic field magnitude of $TE_4$ modes in 610 nm-radius cylindrical resonators with **a**, 0, **b**, 2, and **c**, 3 bridges.

Using this scheme, we compare cases when the bridges enhance or suppress the WGMs with $m$=4. Fig. 5 illustrates the field distribution of the $TE_4$ mode with a different number of bridges. Cases corresponding to 0, 2, 4, and 8 bridges are presented in Fig. 5a. As these numbers, except for 0, are the divisor of 8 (=2$m$), these bridge configurations lift the degeneracy and guarantee one high quality factor mode in the same manner as Fig. 4b. The normalized field distribution of high quality factor modes is given in Fig. 5a. On the other hand, as shown in Fig. 5b, if the number of bridges breaks the 8-fold symmetry of the $TE_4$ mode pattern, bridges deform the field distribution compared to the simple cylinder case, and this significantly decreases the quality factor from 549 to less than 95. Interestingly, if bridges are placed at every |E| antinodes of TE WGM, the quality factor increases from 549 to 749 as clearly seen in the case of 8 bridges in Fig. 5a. Considering the $TE_5$ mode, the quality factor is increased by up to 55% from 2568 (0 bridges) to 3981 (10 bridges).

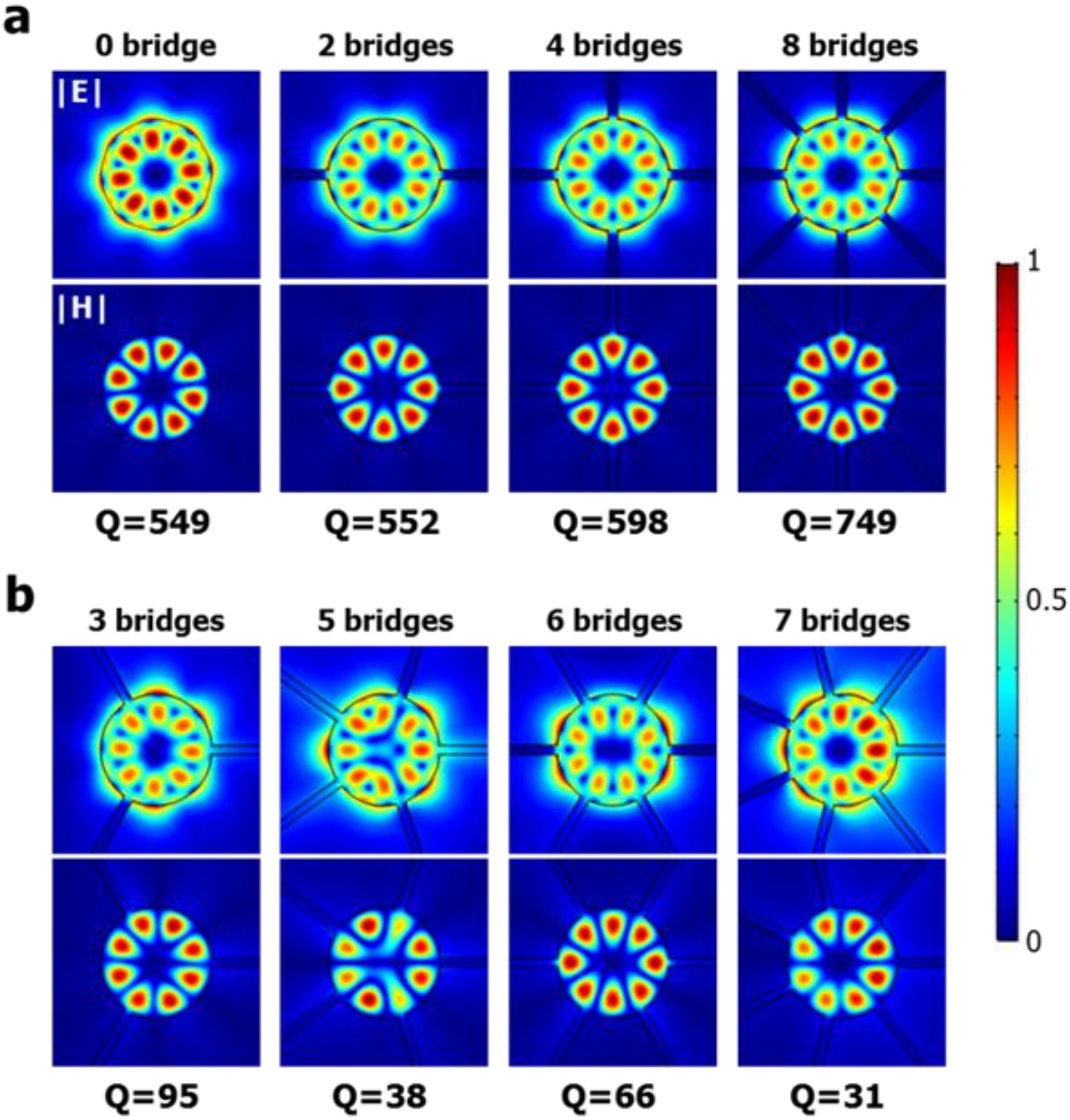

**Fig. 5**. Effect of bridges on the field profile of the WGM. Normalized electric and magnetic field distribution of $TE_4$ mode for a cylindrical resonator of radius R=610 nm with the number of bridges **a**, matching the azimuthal index of the mode (0, 2, 4, and 8 bridges) and **b**, mismatching the azimuthal index of the mode (3, 5, 6, and 7 bridges). The quality factor Q of modes is indicated.

Table 1 tabulates the quality factors of $TE_3$, $TE_4$, $TE_5$, and $TE_6$ modes depending on the number of the bridges which are equally distributed in terms of rotation. Note that the radius is set to have each resonant mode at 1550 nm, which overlaps with the gain peak of wafers. Here, all cases matching between bridge configuration and WGM are noted as bold. In the same manner, we could observe that when the number of bridges is the divisor of the number of antinodes, then the quality factor is preserved. On the other hand, when the number is not the divisor, the quality factor is significantly decreased in all cases. For example, in the case of $TE_6$ mode which has 12 antinodes, 0, 2, 3, 4, 6, and 12 bridges protect the quality factor of modes, while 5, 7, 8, and 10 bridges kill the modes.

| Mode / # of Bridges | $TE_3$ mode (R=510nm) | $TE_4$ mode (R=610nm) | $TE_5$ mode (R=710nm) | $TE_6$ mode (R=810nm) |
|---|---|---|---|---|
| 0 (cylinder) | **112** | **549** | **2568** | **11738** |
| 2 | **118** | **552** | **2448** | **11481** |
| 3 | **125** | 95 | 147 | 2222 |
| 4 | 22 | **598** | 143 | **11527** |
| 5 | 25 | 38 | 501 | 119 |
| 6 | **141** | 66 | 70 | **13230** |
| 8 | 11 | **749** | 98 | 145 |
| 10 | 11 | 13 | **3981** | 79 |
| 12 | 10 | 12 | 14 | **21020** |

**Table 1.** Quality factors of $TE_3$, $TE_4$, $TE_5$, and $TE_6$ modes depending on the number of the bridges.

## 2.3 Experimental demonstration of arbitrary mode selection in microdisk lasers

Using the arbitrary mode selection scheme presented in the previous section, we experimentally demonstrate the mode selectable microdisk lasers. We follow typical nanofabrication steps to fabricate a single resonator suspended in the air.[37] 300nm-thick InGaAsP MQWs are epitaxially grown on an InP wafer. 10 nm wells and 20 nm barriers are alternating 9 times and the composition ratio between the III and IV group is designed to have the most gain around near-IR (~1.5 μm). The exact layer compositions are summarized in Table 2. The overall fabrication steps mainly consist of two steps, which are patterning and suspension, and are summarized in Fig. 6. Fabrication begins with cleaning sample through sonication in order of acetone, then isopropyl alcohol, and finally distilled water for 10 min each. The negative tone hydrogen silsesquioxane (HSQ) e-beam resist (XR1541-006), with high selectivity to the subsequent plasma etching, is spin-coated with a 200 nm thickness. The high-resolution e-beam lithography using the Vistec EBPG5200 writer defines a submicron fine pattern of a cylindrical resonator and its supporting bridges (Fig. 6a). After developing in TMAH solution for one minute, we dry etch the InGaAsP and InP layers to transfer pattern the resonator and the bridges from the developed resist (Fig. 6b). We use the reactive ion etching tool with a plasma of $H_2$, $CH_4$, and Ar for 550 s to etch about 500 nm. Etch depth should be more than 300 nm at least, which is the thickness of the InGaAsP slab, for the subsequent suspending process. After $O_2$ plasma cleaning for 5 min to remove the residuals and removing e-beam resist by a buffered oxide etch (BOE) process (Fig. 6c), a 1.5 μm-thick NR9-1500PY negative tone photoresist is spin-coated, followed by light exposure for 20 s using a mask aligner (Karl Suss MA-6) as shown in Fig. 6d. This process creates an opening to expose the area to suspend and protect the InP layer from unnecessary wet etching. We suspend the resonator by selective wet etching the sacrificial layer for 90s with an HCl solution, which does not react with InGaAsP mostly but with the InP layer (Fig. 6e). After putting the sample in PG remover at 80 °C overnight to remove the photoresist, our device is finalized (Fig. 6f).

| Material | Thickness | Remarks |
|---|---|---|
| InP | 10 nm | Capping layer |
| 1.3Q $In_{1-x}Ga_xAs_yP_{1-y}$ | 30 nm | Barrier (x=0.263, y=0.569) |
| 1.6Q $In_{1-x}Ga_xAs_yP_{1-y}$ | 10 nm | Well (x=0.436, y=0.933), 9 times repeating |
| 1.3Q $In_{1-x}Ga_xAs_yP_{1-y}$ | 20 nm | Barrier (x=0.263, y=0.569), 9 times repeating |
| InP | 1500 nm | Sacrificial layer |
| (100) InP substrate | | Substrate |

**Table 2.** Detailed wafer layers designed to have a maximum gain at 1.55 μm.

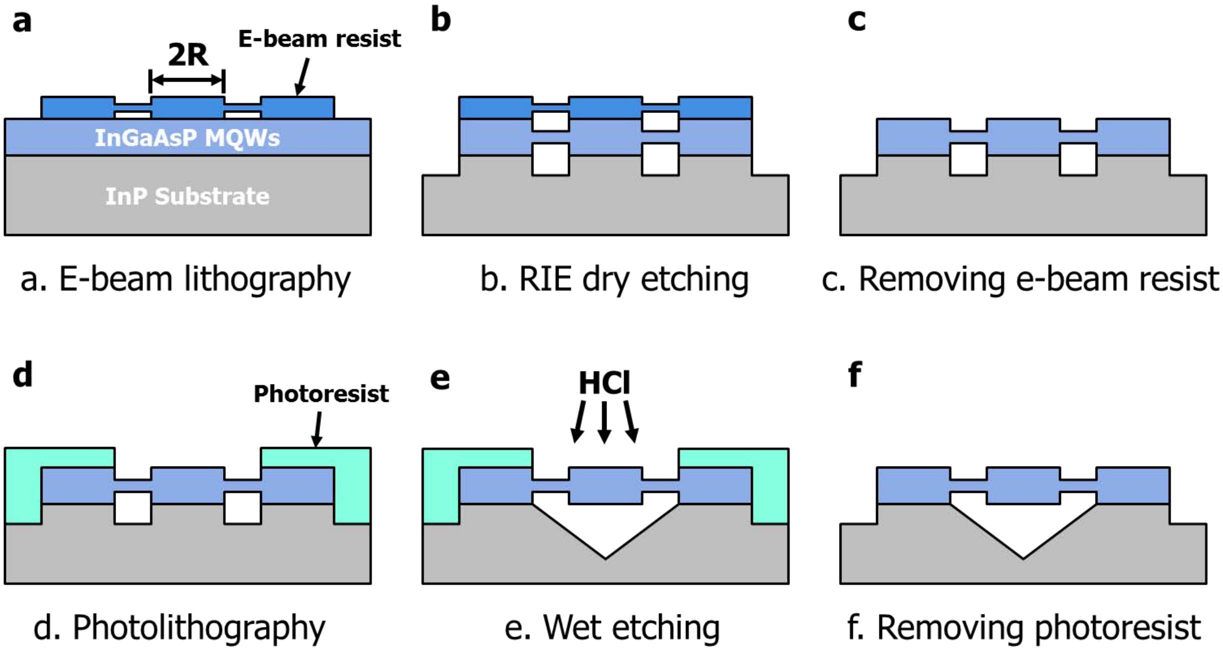

**Fig. 6.** Fabrication process of a self-suspended microdisk resonator. **a**, **b**, **c** Electron beam lithography followed by dry etching to transfer pattern from the resist to wafers. **d, e, f** Selective wet etching to suspend the resonator membrane.

One of the main roadblocks in fabricating suspended microdisks was to transfer exactly electron beam resist patterns to wafers using RIE. When the open gap between the resists is small as a few hundred nanometers scale, the byproduct of etched material during the dry etching step is not efficiently vented out and this causes a nonuniform dry etch rate. This effect is the so-called loading effect and can deform the ideal pattern as dry etching laterally shrinks the pattern as well. As an example, Fig 7 (left) illustrates a microdisk with 12 bridges to optimize the $TE_6$ mode. As shown in the schematic, the gap between two neighboring bridges is gradually reduced near the perimeter of the disk. Due to the loading effect described above, the transferred pattern from the resist to the wafer gets deformed especially near the disk. The red dashed line in the schematic is the expected profile of a dry-etched wafer, and it is shown as a star shape rather than a circle in the right top-view scanning electron microscopic (SEM) image after dry etching and suspension. To address this issue, we decreased the dry etching time while maintaining suspension, and more importantly, we made a compensation in the lithography step.

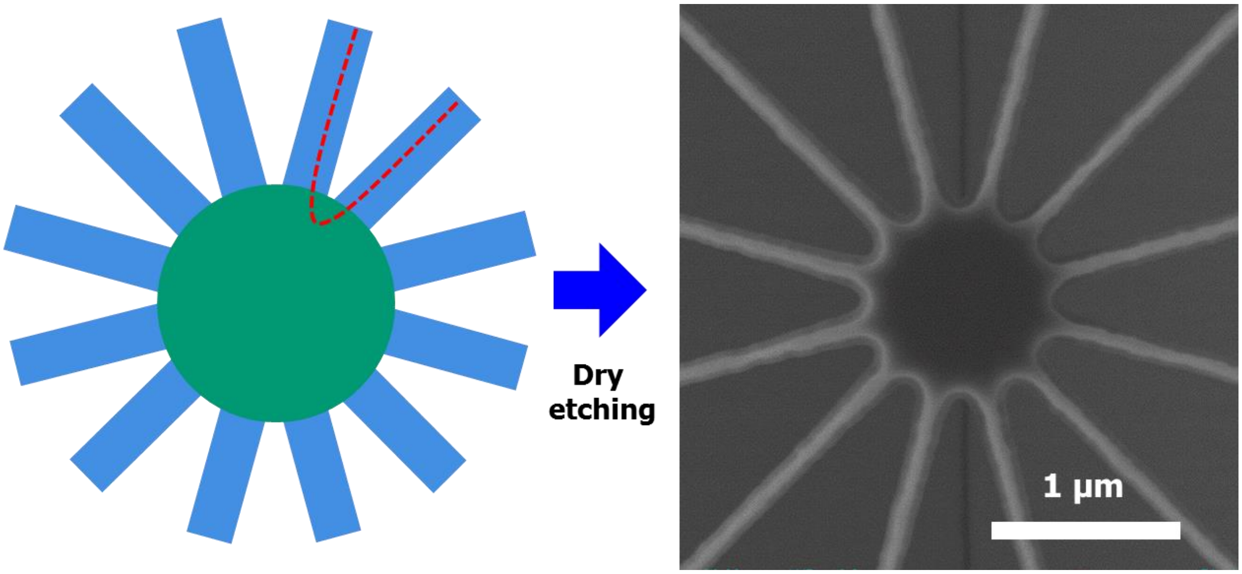

**Fig. 7.** Schematic of microdisk resonator with twelve bridges of mask layout (left) and SEM micrograph of actual device fabricated (right). The Red dashed line represents the expected etching profile.

To explain and verify the effect of manual compensation in the E-beam lithography step, we compared two microdisks with eight bridges as an example. Fig. 8a and b (top) present the mask designs without and with compensation, respectively. As shown in Fig. 8b, the width of bridges is narrowed as they get closer to the disk when compensated manually. This is to maintain the gap between two neighboring bridges large enough and to reduce the loading effect and the subsequent lateral shrinkage. The SEM images of microdisks, as shown at the bottom of Fig 8a and b, devices clearly show improvement in fabrication. This also results in significant distinction in the emission spectrum measurement as shown in the insets of emission spectra measured. The device from Fig.8a (not compensated) doesn't lase while the device from Fig.8b (compensated) does.

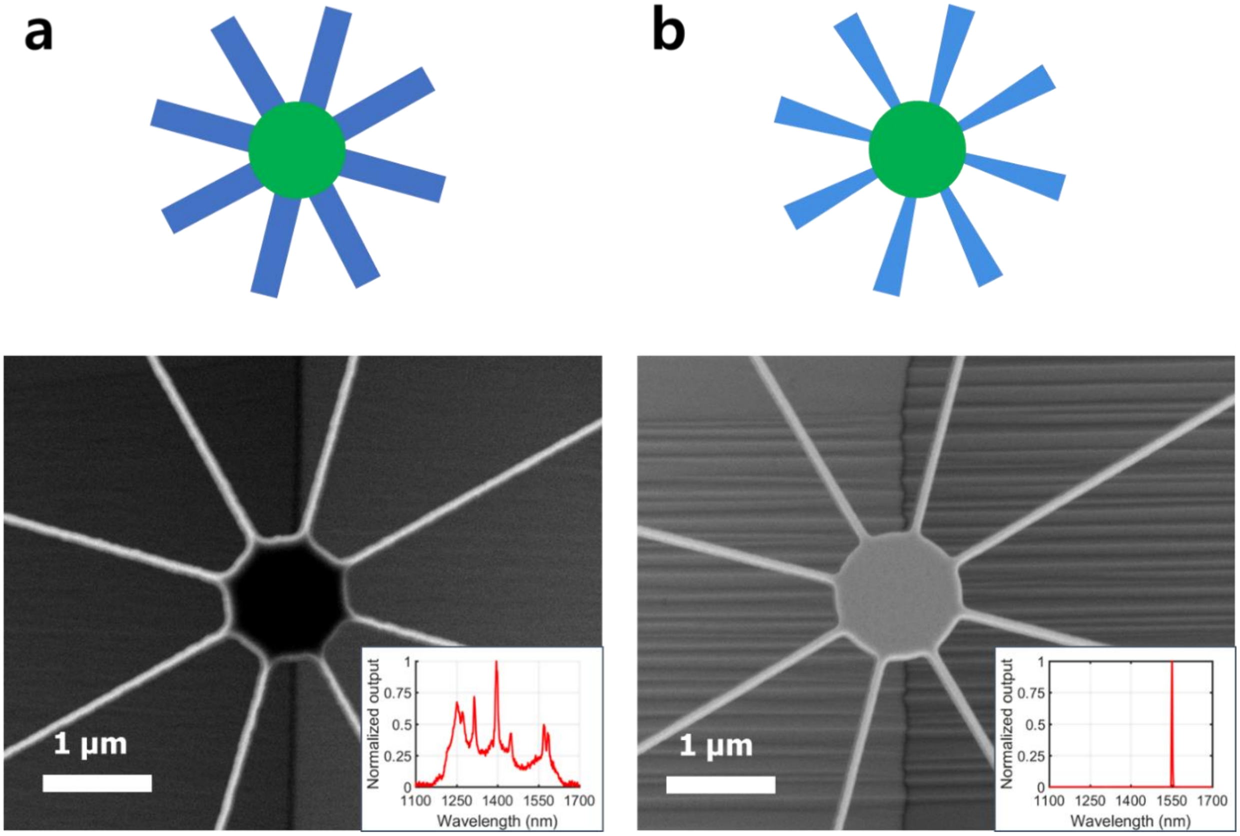

**Fig. 8.** Schematic of microdisk resonator with eight bridges of mask layout (top), and SEM micrograph of actual device fabricated (bottom) without compensation (**a**), and with compensation (**b**). Insets present emission spectrum measured from each device.

Fig. 9 shows the SEM image of a fabricated structure using the process including the compensation. A cylindrical InGaAsP MQWs resonator with 4 bridges is self-suspended in the air with vertical side walls and smooth boundaries. The suspended resonator is optically pumped (purple beam) and the emission from the device is measured for resonators of different radii and the number of bridges. Note that the zoom-in SEM images, shown in Fig. 9b and c, are used to compare the geometrical parameters of the samples to the theoretical specifications.

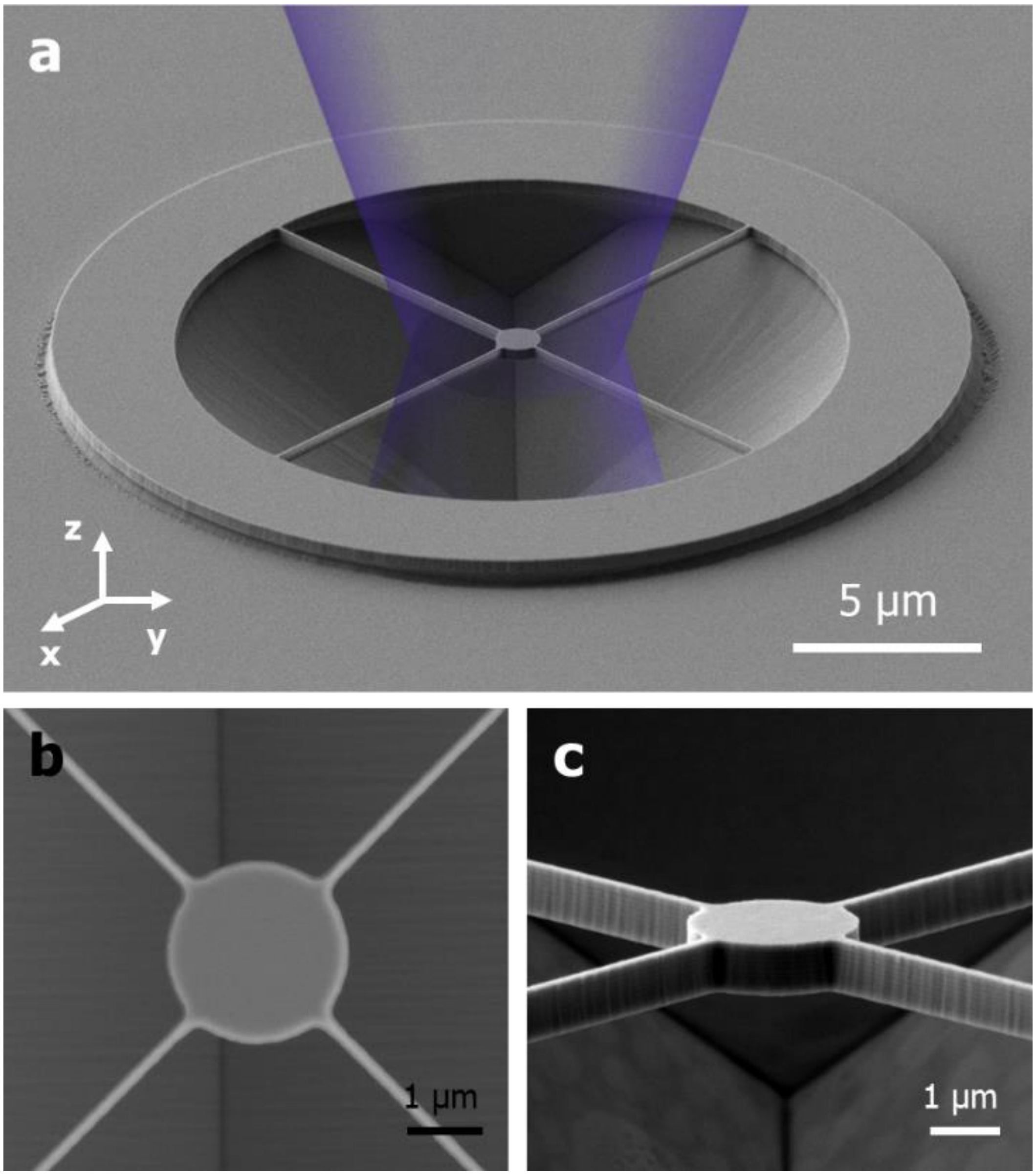

**Fig. 9.** Self-suspended microdisk resonator with four bridges. **a**, Tilted SEM micrograph of a self-suspended device. The purple beam represents the optical pump beam. **b**, Zoom-in top and **c**, tilted view of SEM images of the suspended resonator.

To experimentally compare the responses of resonators in different bridge configurations, the emission spectra are measured using a micro-photoluminescence setup. To optically pump suspended resonators, a 1064 nm pulsed laser with 12 ns pulse width and 215 kHz repetition rate is used at room temperature. The pumping beam is focused onto the sample after passing through the microscope objective with the numerical aperture of 0.4. Emitted light from the sample propagates through the double 4-f lens system and is finally focused either on the InGaAs detector or near-infrared camera by using a flip mirror. The grating-based monochromator was used to measure photoluminescence by the detector at a discrete wavelength with a resolution of 0.33 nm. Fig. 10 presents the normalized photoluminescence as a function of both the radius and the wavelength in the cases of 2 and 4 bridges measured with the same input power. Each column of Fig. 10a and b at a given radius is a spectrum measured from a device. The radius of suspended microdisks is varied from 400 nm to 800 nm with a step of 10 nm and a total of 82 devices are measured in Fig. 10a and b. The insets represent top-view SEM images of one of the measured resonators. It should be noted that 2 bridges placed at 180° from each other do not change the mode pattern of any WGM as they all have at least two nodes. Therefore, any TE WGM with *m* from 3 to 6 appears in Fig. 10a. WGMs with larger *m* have higher quality factors and thus are likely to lase if they are in the gain bandwidth of InGaAsP (see Fig. 3). As a result, with cylinders of a larger radius, higher order WGMs first start to lase. In the case of 4 bridges, however, the $TE_3$ and the $TE_5$ mode are significantly suppressed, while $TE_4$ and $TE_6$ modes are protected. As explained, this stems from the fact that the configuration of bridges significantly affects the field profile of WGMs depending on m. In the non-lasing regime, not only high-Q TE WGMs are observed in Fig. 10, but TM WGMs also appear. However, TM WGMs have lower quality compared to TE WGMs with the same azimuthal index, and the difference in quality factor increases for a larger radius of cylinders as illustrated in Fig. 2b.

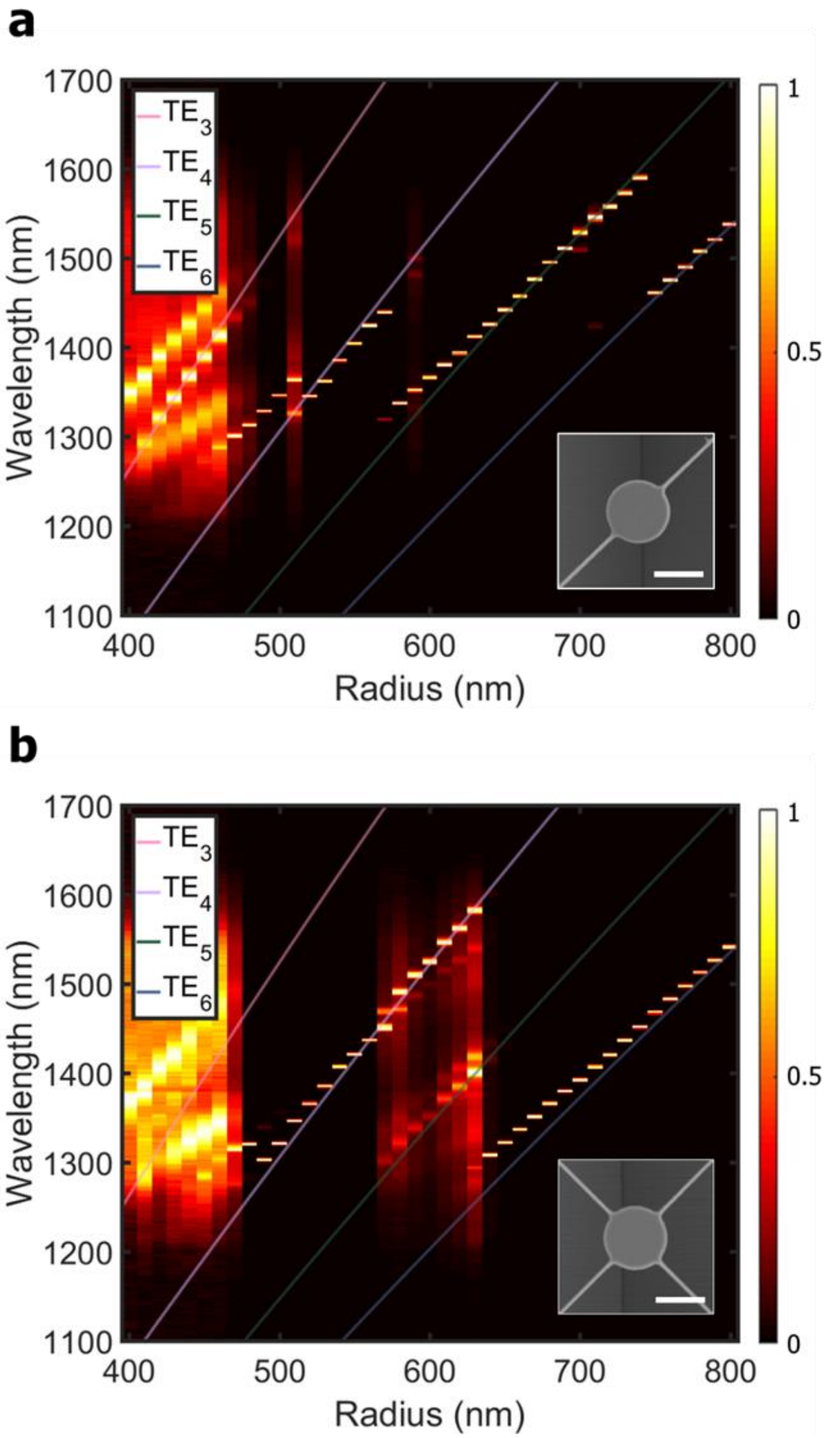

**Fig. 10.** Measured and normalized output power from suspended resonators as a function of the wavelength and the radius of resonators **a**, with 2 bridges, and **b**, with 4 bridges. The resonant

wavelength of four TE WGMs ($m = 3$ to 6) from Fig. 2a is also presented to compare experimental results with the numerical simulation. Insets show SEM images of measured resonators with 1 µm scale bars. Lines are eyes guide and clearly show how the measured emission wavelength changes with the radius.

Using the approach, we demonstrate single-mode microdisk lasers by choosing a suitable number of bridges at the desired wavelength. Fig. 11a and c represent normalized emission spectra of devices with radii of 610 and 710 nm, respectively, designed to have $TE_4$ and $TE_5$ mode with the resonant wavelength at 1.55 µm (see Fig. 1c). As discussed, a WGM has the highest quality factor when the number of bridges is the same as the number of antinodes or $2m$. These resonators are designed to have 8 and 10 bridges to have an optimal quality factor. For comparison, the 2-bridge case is selected as a reference to illustrate the effect of bridges on the lasing mode. Red curves in Fig. 11a and c represent the optimized bridge configurations, while blue curves correspond to the 2-bridge cases. The position of bridges is uniformly distributed but avoids the crystal plane of InP because of possible difficulties in removing the sacrificial InP layer in wet-etching. Insets show top-view SEM images from the characterized device with a different number of bridges. In Fig. 11a, the 2-bridge case shows lasing action at the undesired wavelength (~1.4 µm) due to the appearance of a higher-order WGM ($TE_5$). However, with 8 bridges, single-mode lasing is observed at telecommunication wavelength due to suppression of other existing WGMs with different azimuthal orders $m$. In the case of the resonator of a 710 nm radius (Fig 11c), the device shows single-mode lasing at 1.55 µm as well, whereas microdisks with 2 bridges show lasing actions at different wavelengths. Since the cylindrical resonator with 2 bridges has the same modal response as a pure WGMs, the 2-bridge resonator exhibits other high-Q WGMs which parasitically contribute to multimode lasing. We also measured light-light characteristics and threshold powers of the two laser devices operating at 1.55 µm. Fig. 11b and d correspond to 610 and 710 nm cylindrical resonators with optimized bridge configurations. A clear transition from spontaneous emission to stimulated emission is observed in both cases, confirming that reported devices are indeed lasers.

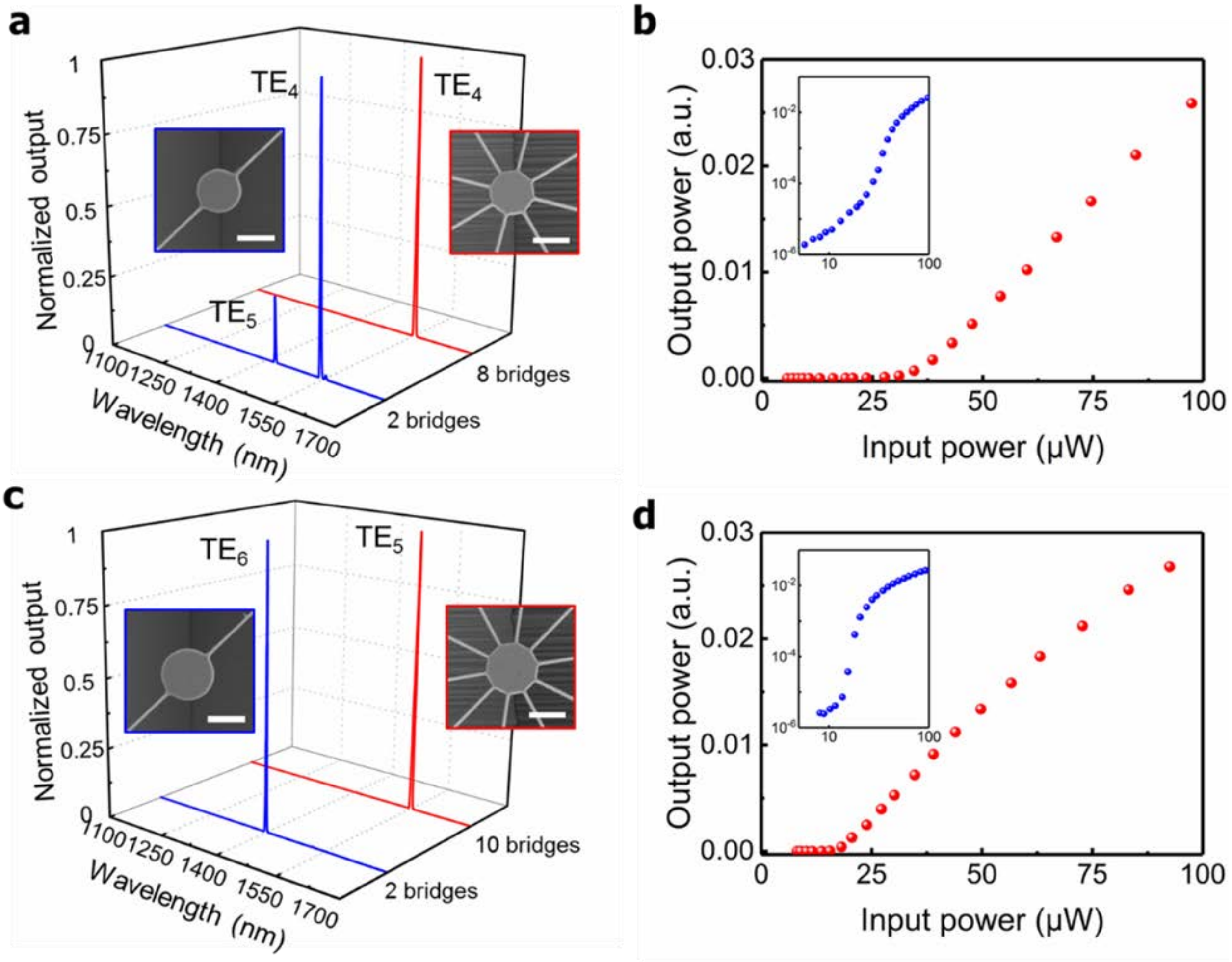

**Fig. 11.** Normalized emission spectra measured from self-suspended microdisks having radius of **a**, 610 nm and **c**, 710 nm designed to support the $TE_4$ and $TE_5$ mode, respectively, at 1.55 μm wavelength. The blue line corresponds to the 2-bridge case used as a reference, while red line corresponds to the optimized bridge configurations with 8 and 10 bridges. Insets show SEM images of measured devices and the scale bars represent 1 μm. Light-light curves clearly show a threshold behavior of the emitted power as a function of pump power, i.e., lasing from optimized devices exploiting **b**, the $TE_4$ and **d**, the $TE_5$ mode. Insets represent log-scale light-light plots.

We proposed and demonstrated self-suspended microdisk lasers via bridges. The bridges play two important roles. They facilitate the mechanical stability of the devices and also provide higher wave confinement on the cavity due to the large refractive index contrast with the environment. More importantly, the bridges can be used to spatially control the field profile of WGMs and therefore to control their quality factor by protecting or breaking their fundamental $2m$-fold rotational symmetry. By controlling the quality factor of WGMs from the configuration of the optimal bridges, we have demonstrated single-mode lasing devices that exploit the $TE_4$ and the $TE_5$ WGMs at telecommunication wavelength. Our approach can be used to engineer WGMs of arbitrary order and is expected to serve as a useful scheme for single-mode lasing in various platforms.

# References

1 Humar, M., Seok Hyun, Y. Intracellular Microlasers. *Nat. Photonics* **9**, 572–576 (2015).
2 Wen, X., Dagan, S., Wysocki, V. H. Small-Molecule Analysis with Silicon-Nanoparticle-Assisted Laser Desorption/Ionization Mass Spectrometry. *Anal. Chem.* **79**, 434–444 (2007).
3 Jackson, S. D. Towards High-Power Mid-Infrared Emission from a Fibre Laser. *Nat. Photonics* **6**, 423–431 (2012).
4 Noll, R., Bette, H., Brysch, A., Kraushaar, M., Mönch, I., Peter, L., Sturm, V. Laser-Induced Breakdown Spectrometry — Applications for Production Control and Quality Assurance in the Steel Industry. *Spectrochi. Acta B* **56**, 637–649 (2001).
5 Staude, I., Miroshnichenko, A. E., Decker, M., Fofang, N. T., Liu, S., Gonzales, E., Dominguez, J., Luk, T. S., Neshev, D. N., Brener, I. Tailoring Directional Scattering through Magnetic and Electric Resonances in Subwavelength Silicon Nanodisks. *ACS Nano* **7**, 7824–7832 (2013).
6 Sheikholeslami, S. N., García-Etxarri, A., Dionne, J. A. Controlling the Interplay of Electric and Magnetic Modes via Fano-like Plasmon Resonances. *Nano Letters* **11**, 3927–3934 (2011).
7 Aouani, H., Mahboub, O., Bonod, N., Devaux, E., Popov, E., Rigneault, H., Ebbesen, T. W., Wenger, J. Bright Unidirectional Fluorescence Emission of Molecules in a Nanoaperture with Plasmonic Corrugations. *Nano Letters* **11**, 637–644 (2011).
8 Liu, Y., Zentgraf, T., Bartal, G., Zhang, X. Transformational Plasmon Optics. *Nano Letters* **10**, 1991–1997 (2010).
9 Bahari, B., Ndao, A., Vallini, F., Amili, A. E., Fainman, Y., Kanté, B. Nonreciprocal Lasing in Topological Cavities of Arbitrary Geometries. *Science* **358**, 636-640 (2017).
10 Hill, M. T., Gather, M. C. Advances in Small Lasers. *Nat. Photonics* 2014, 8, 908–918.
11 Noda, S. Seeking the Ultimate Nanolaser. *Science* **314**, 260–261 (2006).
12 Iga, K., Koyama, F., Kinoshita, S. Surface Emitting Semiconductor Lasers. *IEEE J. Quantum Electron.* **24**, 1845–1855 (1988).
13 Koyama, F. Recent Advances of VCSEL Photonics. *J. Light. Technol.* **24**, 4502–4513 (2006).
14 Lorenser, D., Unold, H. J., Maas, D. J. H. C., Aschwanden, A., Grange, R., Paschotta, R., Ebling, D., Gini, E., Keller, U. Towards Wafer-Scale Integration of High Repetition Rate Passively Mode-Locked Surface-Emitting Semiconductor Lasers. *Appl. Phys. B* **79**, 927–932 (2004).
15 McCall, S. L., Levi, A. F. J., Slusher, R. E., Pearton, S. J., Logan, R. A. Whispering-gallery Mode Microdisk Lasers. *Appl. Phys. Lett.* **60**, 289–291 (1992).
16 Song, Q., Cao, H., Ho, S. T., Solomon, G. S. Near-IR Subwavelength Microdisk Lasers. *Appl. Phys. Lett.* **94**, 061109 (2009).
17 Zhang, Z., Yang, L., Liu, V., Hong, T., Vahala, K., Scherer, A. Visible Submicron Microdisk Lasers. *Appl. Phys. Lett.* **90**, 111119 (2007).
18 Liu, Z., Shainline, J. M., Fernandes, G. E., Xu, J., Chen, J., Gmachl, C. F. Continuous-Wave Subwavelength Microdisk Lasers at $\lambda = 1.53$ Mm. *Opt. Express* **18**, 19242–19248

(2010).
19 Salehzadeh, O., Djavid, M., Tran, N. H., Shih, I., Mi, Z. Optically Pumped Two-Dimensional MoS2 Lasers Operating at Room-Temperature. *Nano Letters* **15**, 5302–5306 (2015).
20 Chen, R., Gupta, S., Huang, Y.-C., Huo, Y., Rudy, C. W., Sanchez, E., Kim, Y., Kamins, T. I., Saraswat, K. C., Harris, J. S. Demonstration of a Ge/GeSn/Ge Quantum-Well Microdisk Resonator on Silicon: Enabling High-Quality Ge(Sn) Materials for Micro- and Nanophotonics. *Nano Letters* **14**, 37–43 (2014).
21 Stange, D., Wirths, S., Geiger, R., Schulte-Braucks, C., Marzban, B., von den Driesch, N., Mussler, G., Zabel, T., Stoica, T., Hartmann, J.-M., et al. Optically Pumped GeSn Microdisk Lasers on Si. *ACS Photonics* **3**, 1279–1285 (2016).
22 Akahane, Y., Asano, T., Song, B.-S., Noda, S. High-Q Photonic Nanocavity in a Two-Dimensional Photonic Crystal. *Nature* **425**, 944–947 (2003).
23 Lončar, M., Yoshie, T., Scherer, A., Gogna, P., Qiu, Y. Low-Threshold Photonic Crystal Laser. *Appl. Phys. Lett.* **81**, 2680–2682 (2002).
24 Lepetit, T., Kanté, B. Controlling Multipolar Radiation with Symmetries for Electromagnetic Bound States in the Continuum. *Phys. Rev. B* **90**, 241103(R) (2014).
25 Kodigala, A., Lepetit, T., Gu, Q., Bahari, B., Fainman, Y., Kanté, B. Lasing Action from Photonic Bound States in Continuum. *Nature* **541**, 196–199 (2017).
26 Nezhad, M. P., Simic, A., Bondarenko, O., Slutsky, B., Mizrahi, A., Feng, L., Lomakin, V., Fainman, Y. Room-Temperature Subwavelength Metallo-Dielectric Lasers. *Nat. Photonics* **4**, 395–399 (2010).
27 Yu, K., Lakhani, A., Wu, M. C. Subwavelength Metal-Optic Semiconductor Nanopatch Lasers. *Opt. Express* **18**, 8790–8799 (2010).
28 Oulton, R. F., Sorger, V. J., Zentgraf, T., Ma, R.-M., Gladden, C., Dai, L., Bartal, G., Zhang, X. Plasmon Lasers at Deep Subwavelength Scale. *Nature* **461**, 629–632 (2009).
29 Noginov, M. A., Zhu, G., Belgrave, A. M., Bakker, R., Shalaev, V. M., Narimanov, E. E., Stout, S., Herz, E., Suteewong, T., Wiesner, U. Demonstration of a Spaser-Based Nanolaser. *Nature* **460**, 1110–1112 (2009).
30 He, L., Özdemir, Ş. K., Yang, L. Whispering Gallery Microcavity Lasers. *Laser & Photonics Rev.* **7**, 60–82 (2013).
31 Little, B. E., Laine, J.-P., Chu, S. T. Surface-Roughness-Induced Contradirectional Coupling in Ring and Disk Resonators. *Opt. Lett.* **22**, 4–6 (1997).
32 Fujita, M., Baba, T. Microgear Laser. *Appl. Phys. Lett.* **80**, 2051–2053 (2002).
33 Bogdanov, A. A., Mukhin, I. S., Kryzhanovskaya, N. V., Maximov, M. V., Sadrieva, Z. F., Kulagina, M. M., Zadiranov, Y. M., Lipovskii, A. A., Moiseev, E. I., Kudashova, Y. V., et al. Mode Selection in InAs Quantum Dot Microdisk Lasers Using Focused Ion Beam Technique. *Opt. Lett.* **40**, 4022–4025 (2015).
34 Moiseev, E. I., Kryzhanovskaya, N., Polubavkina, Y. S., Maximov, M. V., Kulagina, M. M., Zadiranov, Y. M., Lipovskii, A. A., Mukhin, I. S., Mozharov, A. M., Komissarenko, F. E., et al. Light Outcoupling from Quantum Dot-Based Microdisk Laser via Plasmonic Nanoantenna. *ACS Photonics* **4**, 275–281 (2017).
35 Kryzhanovskaya, N., Polubavkina, Y., Moiseev, E., Maximov, M., Zhurikhina, V.,

Scherbak, S., Lipovskii, A., Kulagina, M., Zadiranov, Y., Mukhin, I., et al. Enhanced Light Outcoupling in Microdisk Lasers via Si Spherical Nanoantennas. *J. Appl. Phys.* **124**, 163102 (2018).
36 Feng, L., Wong, Z. J., Ma, R.-M., Wang, Y., Zhang, X. Single-Mode Laser by Parity-Time Symmetry Breaking. *Science* **346**, 972–975 (2014).
37 Hodaei, H., Miri, M.-A., Heinrich, M., Christodoulides, D. N., Khajavikhan, M. Parity-Time–Symmetric Microring Lasers. *Science* **346**, 975–978 (2014).
38 Zhukovsky, S. V., Chigrin, D. N., Lavrinenko, A. V., Kroha, J. Switchable Lasing in Multimode Microcavities. *Phys. Rev. Lett.* **99**, 073902 (2007).
39 Kodigala, A., Gu, Q., Lepetit, T., Bahari, B., Kanté, B. Mechanically Stable Conjugate and Suspended Lasing Membranes of Bridged Nano-Cylinders. *Opt. Mater. Express* **7**, 2980–2992 (2017).
40 Blair, S., Chen, Y. Resonant-Enhanced Evanescent-Wave Fluorescence Biosensing with Cylindrical Optical Cavities. *Appl. Opt.* **40**, 570 (2001).
41 Shainline, J., Elston, S., Liu, Z., Fernandes, G., Zia, R., Xu, J. Subwavelength Silicon Microcavities. *Opt. Express* **17**, 23323–23331 (2009).
42 Karouta, F. A Practical Approach to Reactive Ion Etching *J. Phys. D: Appl. Phys*. **47,** 233501 (2014).

# 3

# *Single-Mode Quantum Valley-Hall Effect Topological Laser*[*]

## 3.1 Introduction

The efficient generation, manipulation, and detection of light for applications including sensing, communications, and computing require the control of fundamental degrees of freedom of photons such as the frequency, the polarization, or the momentum[1]. The control of light in integrated photonics platforms has enabled revolutionary devices ranging from optical fibers to lasers and quantum light sources[2]. Two-dimensional crystals with honeycomb lattices have been shown to exhibit an additional degree of freedom known as the valley degree of freedom[3,4]. Valleys are local energy extrema of the Bloch energy band of periodic structures, and, the interband control of energy flow between valleys could enable information processing schemes that are protected by topology[5,6]. Recently, topology has emerged as a powerful design tool to control light at the nanoscale, and, passive devices, difficult or impossible to realize with traditional approaches, have now been reported[7-19]. Topology is thus poised to revolutionize future classical and quantum photonic integrated circuits based on unprecedented transport properties. Although active topological devices exploiting protected edge states have recently been investigated[20], the geometry of current topological platforms is too complex to warrant heterogeneous integration in photonic circuits[21-30]. Moreover, the complex geometries used to create the topological phases

---

[*] * The following section is publishedin Optics Letters. (W. Noh, H. Nasari, H. -M. Kim, Q. Le-Van, Z. Jia, C. -H. Huang, B. Kanté, “Experimental Demonstration of Single-mode Topological Valley-Hall Lasing at Telecommunication Wavelength Controlled by the Degree of Asymmetry”, Optics Letters, 45, 4108-4111, 2020)

leave limited parameters to further control topological modes and their quality factors. For example, the topological laser based on the quantum-Hall effect requires magnetic substrates and has a footprint of ~ 21 by 21 $\lambda^2$ and a threshold density of 0.75 [$\mu$W/$\mu$m$^2$][23]. The laser based on the spin-Hall effect has a footprint of ~ 95 by 95 $\lambda^2$ and a threshold density of 160 [$\mu$W/$\mu$m$^2$][24]. In the two cases, single-mode lasing was achieved using the spectral filtering of the non-trivial topological bandgap in the first case, and, selective spatial pumping of the edge modes in the second case. More recently, a quantum cascade valley-Hall emitting device was reported at terahertz frequencies, but, single-mode operation has not been achieved for the valley-Hall platform[30]. Here, we report valley-Hall topological lasers at telecommunication frequency and demonstrate that the degree of asymmetry (DoA) can be controlled to enable single-mode operation. The DoA, defined as the normalized difference between the radius of large and small holes in the honeycomb lattice with broken inversion symmetry, creates four distinct photon confinement regimes with feedback giving rise to defect-like modes, Fabry-Perot-like modes, and evenly spaced ring-like modes, all confined in the topological bandgap. An interplay between the width of the topological bandgap and the quality factor of ring-like modes controls the single-mode operation.

## 3.2 Optimization of valley-Hall cavity for single-mode lasing by controlling degree of asymmetry

The schematic of a free-standing triangular valley-Hall cavity is shown in Fig. 1. The triangular cavity, indicated in red, is a structured and suspended membrane at the interface between two distinct honeycomb photonic crystal (PhC) lattices of opposite valley-Chern numbers of ±1/2. The unit cell and its parameters are described in the inset. The inversion symmetry of the honeycomb lattices is broken using holes of the different radii ($R_1$ and $R_2$), opening a bandgap at the $K$ and $K'$ valleys in the Brillouin zone. The interface between two topologically distinct PhCs with swapped small (radius $R_1$) and large (radius $R_2$) holes position creates edge modes localized at the interface of PhC I and PhC II. The cavity is fabricated on InGaAsP multiple quantum wells with a gain spectrum over the telecommunication wavelength of 1.55 μm. The structures are fabricated using electron-beam lithography followed by inductively coupled plasma etching of the InGaAsP multiple quantum wells to define the PhCs, and, wet etching to suspend the cavity. Details on fabrication steps will be discussed in the next section.

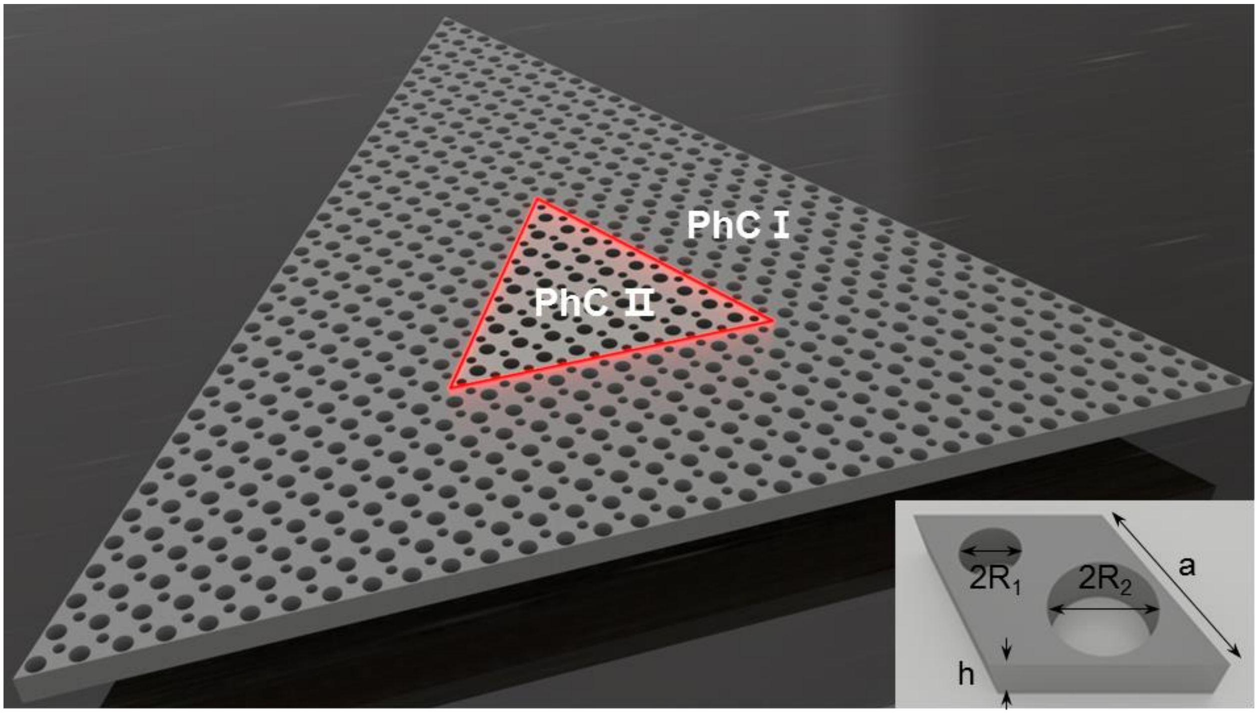

**Fig. 1.** Sketch of a suspended valley-Hall cavity indicated by the red triangle at the interface between two distinct honeycomb photonic crystal (PhC) lattices of opposite valley-Chern numbers of ±1/2. The inversion symmetry of the honeycomb lattices is broken using holes of the different radius ($R_1$ and $R_2$) in the honeycomb lattice, opening a bandgap at the $K$ and $K'$ valleys. Interfacing two topologically distinct PhCs with swapped small (radius $R_1$) and large (radius $R_2$) holes positions creates an edge mode localized at the interface of PhC I and PhC II. The inset presents geometrical parameters.

Fig. 2a presents the band structure of two honeycomb lattices, one with inversion symmetry (blue dash line) and the second with broken inversion symmetry (black solid line). The plots are restricted to the transverse electric (TE) polarization that dominates the dispersion of air-hole-type photonic crystal structures[32]. The orange region, above the light-line, represents the radiation zone. The honeycomb photonic crystal with inversion symmetry has $C_6$ symmetry and exhibits a Dirac cone dispersion at the $K$ and $K'$ points in the first Brillouin zone. By breaking the $C_6$ symmetry, a photonic bandgap, represented by the gray area, appears. In Fig. 2b, the width of the bandgap is calculated as a function of the degree of asymmetry (DoA) defined as

$$DoA = \frac{R_2 - R_1}{a_0} \qquad (1)$$

The degree of asymmetry quantifies the dissimilarity of the large and small holes in the honeycomb lattice, and, as seen, the bandgap widens with the DoA. The interface between two distinct PhCs with swapped small and large holes position constitutes a valley-Hall topological waveguide with edge states. The dispersion of the edge states is calculated using a supercell waveguide. The TE-like band structures are obtained by the finite-element method (COMSOL Multiphysics). Floquet periodic boundary conditions and perfectly matched layer (PML) are applied at the boundary of the structure.

Results, presented in Fig. 2c-e, are obtained for DoAs of 0.07 (Fig. 2c), 0.13 (Fig. 2d), and 0.20 (Fig. 2e). The light-line and bulk bands are indicated as a red dotted line and dark grey areas, respectively. The dispersion curve of the topological mode (purple line) evidences four photon confinement regimes that depend on the DoA. Regime 1 (yellow) corresponds to topological waveguiding below the light cone. Regime 2 (blue) and regime 3 (cyan) correspond to topological waveguiding above the light cone. In regime 2, the propagating mode has a unique wavevector while it has two wavevectors in regime 3. Regime 4 (pink) is a bandgap that does not support any waveguide mode.

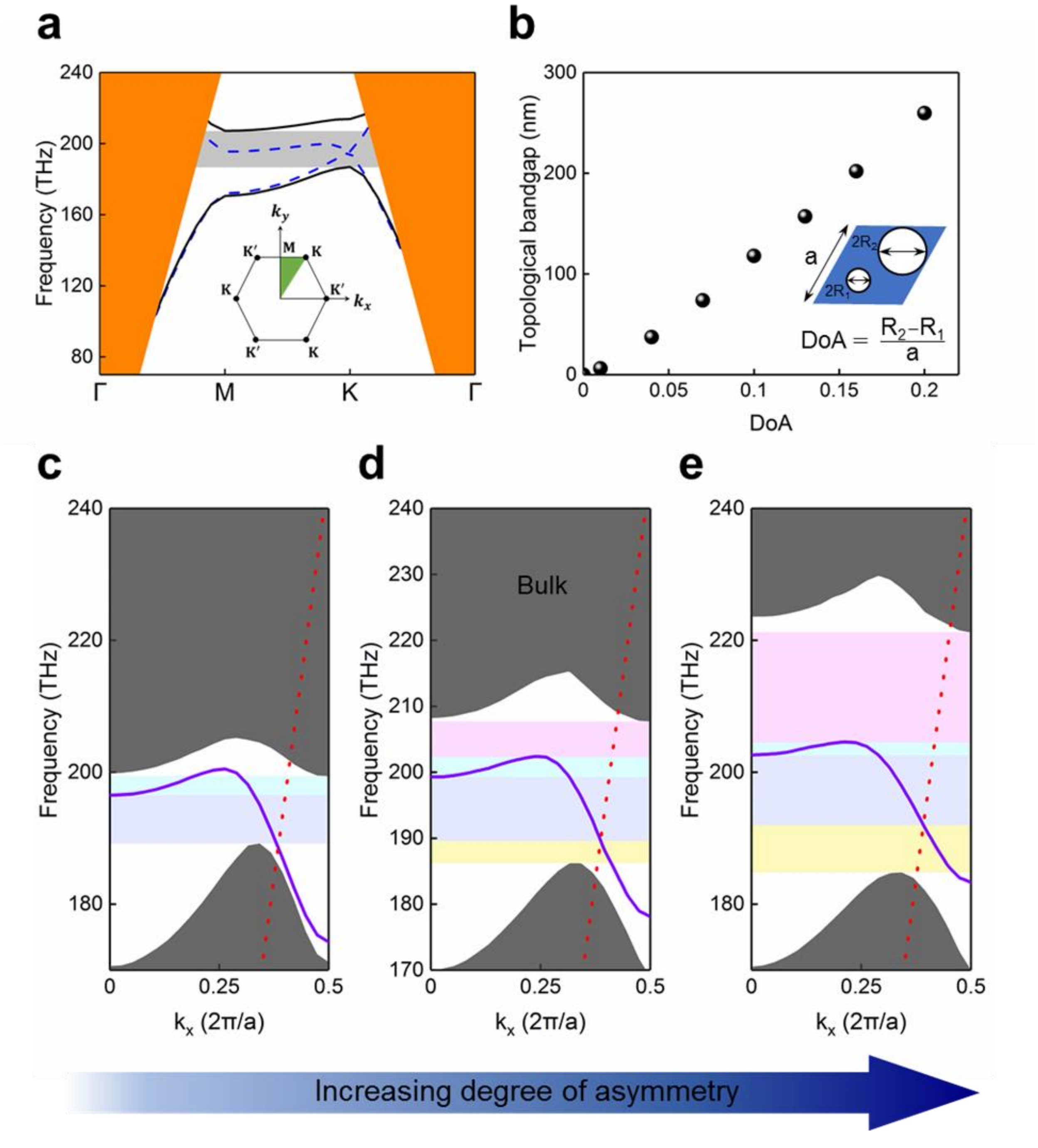

**Fig. 2. a**, Band structure of honeycomb lattices with inversion symmetry (blue dash line) and broken inversion symmetry (black solid line). The orange region represents the radiation zone. The honeycomb photonic crystal structure with $C_6$ symmetry exhibits a Dirac cone dispersion at the *K* and *K'* points in the momentum space. By breaking the $C_6$ symmetry, a photonic bandgap, represented by the gray area, appears. The inset shows the first Brillouin zone of the honeycomb

lattice. **b**, Bandgap as a function of the degree of asymmetry (DoA) defined as DoA = $(R_2 - R_1)\ /\ a_0$). The bandgap widens with the DoA. **c**, **d**, **e**, Band structure of a supercell waveguide, interface of two topologically distinct PhCs with swapped small and large holes position, and DoAs of 0.07 (c), 0.13 (d), and 0.20 (e). The light-line and bulk bands are indicated as red dotted lines and dark grey areas, respectively. The dispersion curve of the topological mode (purple line) evidences four photon confinement regimes controlled by the DoA. Regime 1 (yellow) corresponds to topological waveguiding below the light cone. Regime 2 (blue) and regime 3 (cyan) correspond to topological waveguiding above the light cone. In regime 2 the propagating mode has a single wavevector while it has two wavevectors in regime 3. Regime 4 (pink) does not support any waveguide mode.

To elaborate on how the dispersion curve is obtained, Fig 3a shows the schematic of the supercell of the waveguide. The interface is constructed by swapping the big hole's and small hole's positions of two topologically distinct PhCs with Chern number of $\pm\frac{1}{2}$. The calculated interfacial waveguide structure is shown in Fig. 3b. Note that the vertical boundary conditions are set to periodic in Fig. 3c, the normalized electric-field magnitude, at k=0.5($2\pi$/a), evidences energy confinement at the interface.

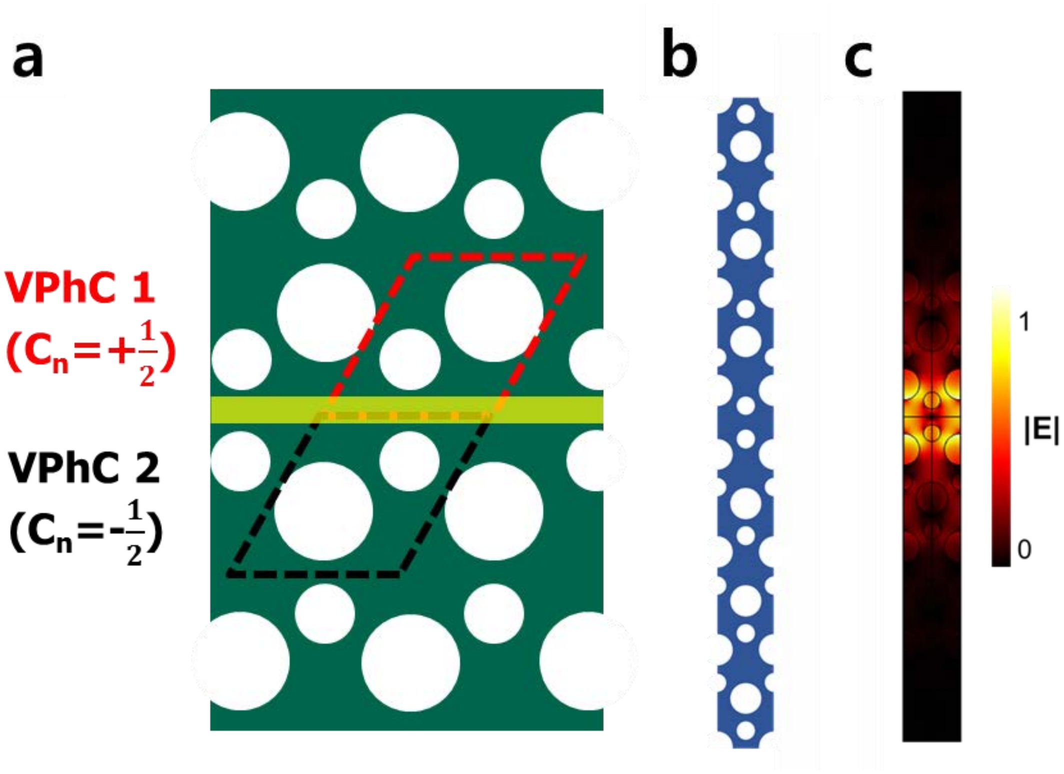

**Fig. 3**. Supercell simulation of valley-Hall waveguide. **a**, Schemtaic of supercell of the valley-Hall waveguide between topologically inverted photonic crystal with the opposite Chern number $\pm\frac{1}{2}$. **b**, Actual structure of the waveguide used in numerical calculation. **c**, Normalized electric-field magnitude (|E|) profile at k=0.5 (2$\pi$/a).

A valley-Hall cavity, for example, the equilateral triangular cavity of Fig. 1, is a closed contour along *ΓK* (*ΓK'*) directions at the interface of the crystals. Light traveling around the contour forms standing waves of various patterns known as modes. Fig. 4 presents the quality factors of modes of the valley-Hall cavity as well as their near-field and far-field patterns. The quality factor of resonant modes of the triangular valley-Hall cavity (side length 36*a*, where *a* is the lattice constant) with a DoA of 0.13 is presented in Fig. 4a. The thickness and lattice constant of the honeycomb lattice photonic crystals are 120 nm and 612 nm, respectively. The refractive index of the InGaAsP slab is 3.4. Modes are calculated using a three-dimensional finite-difference time-domain (FDTD) method using Lumerical. In the yellow region (regime 1) and blue region (regime 2), ring-like modes (RLMs) are observed with a wavelength spacing of about 10 nm. The quality factors of RLMs are larger in the yellow region (regime 1) compared to the blue region (regime 2). The yellow region corresponds to non-radiative modes because wavevectors are located below the light-line while the blue region corresponds to the radiative modes with wavevectors located above the light-line. In the blue region, energy is leaked to the far-field as the wave propagates along the cavity. In the cyan region (regime 3), cavity modes localized at one side of the triangle are observed, and, they are denoted by topological Fabry-Perot modes[33,34]. The pink region (regime 4) corresponds to defect-like modes localized at one vertex of the triangle. To quantify the single-mode nature of the cavity, the highest quality factor in the topological valley-Hall cavity (black line, left axis) is plotted as a function of the DoA. As seen, the quality factor mostly increases with the DoA. We also introduce the figure of merit (FOM) (blue line, right axis) defined as the normalized difference between the highest ($Q_{\mathrm{1st}}$) and the second-highest quality factors ($Q_{\mathrm{2nd}}$) of ring-like modes, i.e.,

$$FOM = \frac{Q_{\mathrm{1st}} - Q_{\mathrm{2nd}}}{Q_{\mathrm{1st}}} \qquad (2)$$

Very interestingly, while $Q_{\mathrm{1st}}$ mostly increases with the DoA, the FOM reaches a maximum and then decreases. This originates from an interplay between the width of the topological gap that increases continuously with the DoA and the quality factor of multiple ring-like modes that become all strongly confined. A larger DoA enlarges the size of the bandgap below the light-cone. This, in turn, increases the momentum mismatch between the cavity mode and light-line, thus decreasing out-of-plane scattering at sharp corners. However, when the DoA is further increased, more modes become confined below light-cone giving rise to mode competition. Fig. 4c-f presents the normalized electric field magnitude in the near-field (top) and the normal Poynting vector in the far-field (bottom) for cavity modes indicated in Fig. 4a as red circles. In Fig. 4c, the RLM is below light-cone, and the far-field exhibit bright vertices due to out-of-plane scattering caused by the abrupt change in shape at the sharp corners. In Fig. 4d, the RLM is above the light-cone and is thus visible both in the near-field and the far-field. In Fig. 4e, topological Fabry-Perot modes above light-cone, localized at one side of the triangle, are visible both in the near-field and the far-field. In this regime, the edge state has a smaller group velocity enabling feedback and localization with only one side of the triangle. In Fig. 4f, a defect mode visible both in the near-field and the far-field is observed due to the sharp bending of the waveguides.

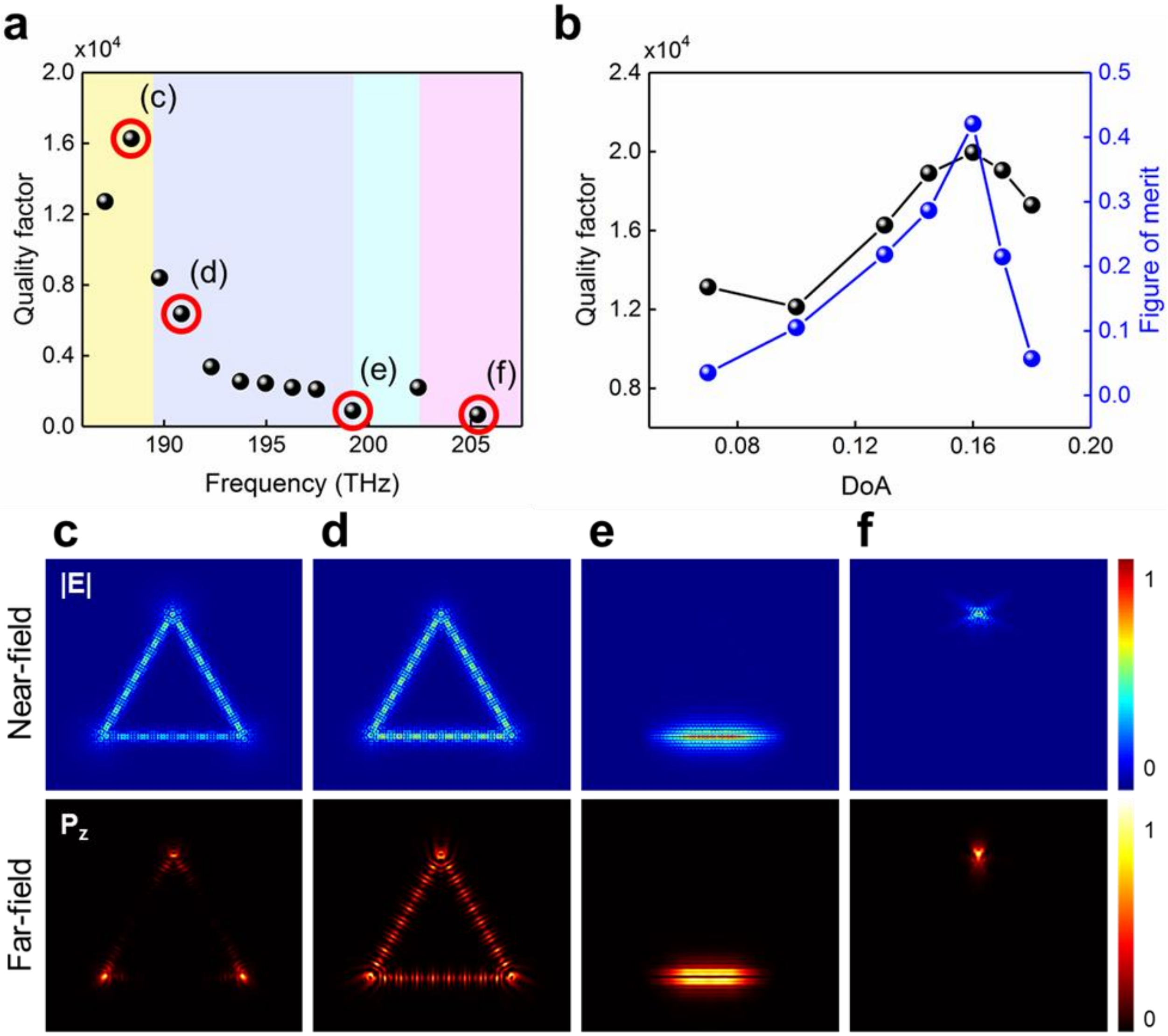

**Fig. 4**. **a**, The quality factor of resonant modes in a representative triangular valley-Hall cavity with a DoA of 0.13. In the yellow region (regime 1) and blue region (regime 2), ring-like modes (RLMs) are observed with a wavelength spacing of about 10 nm. The quality factors of RLMs are larger in the yellow region (regime 1) compared to the blue region (regime 2). The yellow region corresponds to non-radiative modes as their wavevector is located below light-line while the blue region corresponds to radiative modes with wavevectors located above the light-line. In the blue region, energy is leaked to the far-field as the wave propagates along the cavity. The cyan region (regime 3) contains cavity modes localized on one side of the triangle, which are referred to as topological Fabry-Perot modes. The pink region (regime 4) corresponds to defect-like mode localized at one vertex of the triangle. **b**, Highest quality factor in the topological valley-Hall cavity (black line, left axis) as a function of the DoA. The blue line (right axis) represents the figure of

merit (FOM) defined as the normalized difference between the highest ($Q_{1st}$) and the second-highest quality factors ($Q_{2nd}$) of ring-like modes, i.e., FOM= ($Q_{1st}$-$Q_{2nd}$)/$Q_{1st}$. The quality factor of the highest Q mode mostly increases with the DoA, but, the FOM reaches the maximum around DoA=0.16. **c**-**f**, Normalized electric field magnitude in the near-field (top) and normal Poynting vector ($P_z$), i.e., far-field (bottom) for cavities indicated in Fig. 4a **c**, A RLM below the light-cone. In the far-field, vertices are bright due to out-of-plane scattering caused by the abrupt change in shape at the sharp corners of the triangle. **d**, RLM above the light-cone and thus visible both in the near-field and the far-field. **e**, Topological Fabry-Perot mode above light-cone visible both in the near-field and the far-field. **f**, Defect mode visible both in the near-field and the far-field.

## 3.3 Experimental demonstration of single-mode valley-Hall topological laser

The existence of multiple feedback mechanisms in the valley-Hall platform has made the single-mode lasing of this system challenging. To demonstrate single-mode lasing, we have thus fabricated devices around the highest FOM where the separation between competing modes is the largest. The flowchart of the nanofabrication process is illustrated in Fig. 5, which is similar to the fabrication steps discussed here[36,37]. The valley-Hall cavity is prepared on 120 nm-thick InGaAsP multiple quantum wells (MQWs) with a gain spectrum over telecommunication wavelength. Wafer stacks are also the same as the 300 nm MQWs wafers used in microdisk, but there are only three wells. After the InP capping layer is removed, the InGaAsP wafer is cleaned by typical acetone and isopropyl alcohol sonication. Subsequently, hydrogen silsesquioxane (HSQ) negative tone resist is spin-coated on the wafer and the valley-Hall cavity is patterned by electron-beam lithography. In the following step, induced coupled plasma (ICP) dry etching with a mixture of $H_2$, $CH_4$, Ar, and $Cl_2$ gas is performed to transfer the patterns to the InGaAsP. ICP is known to have a higher etch rate and verticality than RIE used in microdisk fabrication. Then the HSQ layer is removed by a buffered oxide etchant (BOE) solution. Subsequently, the areas to be wet-etched are opened in the negative-tone photoresist. Finally, the device is suspended by a diluted HCl (3:1) solution which selectively removes the InP sacrificial layer under the InGaAsP.

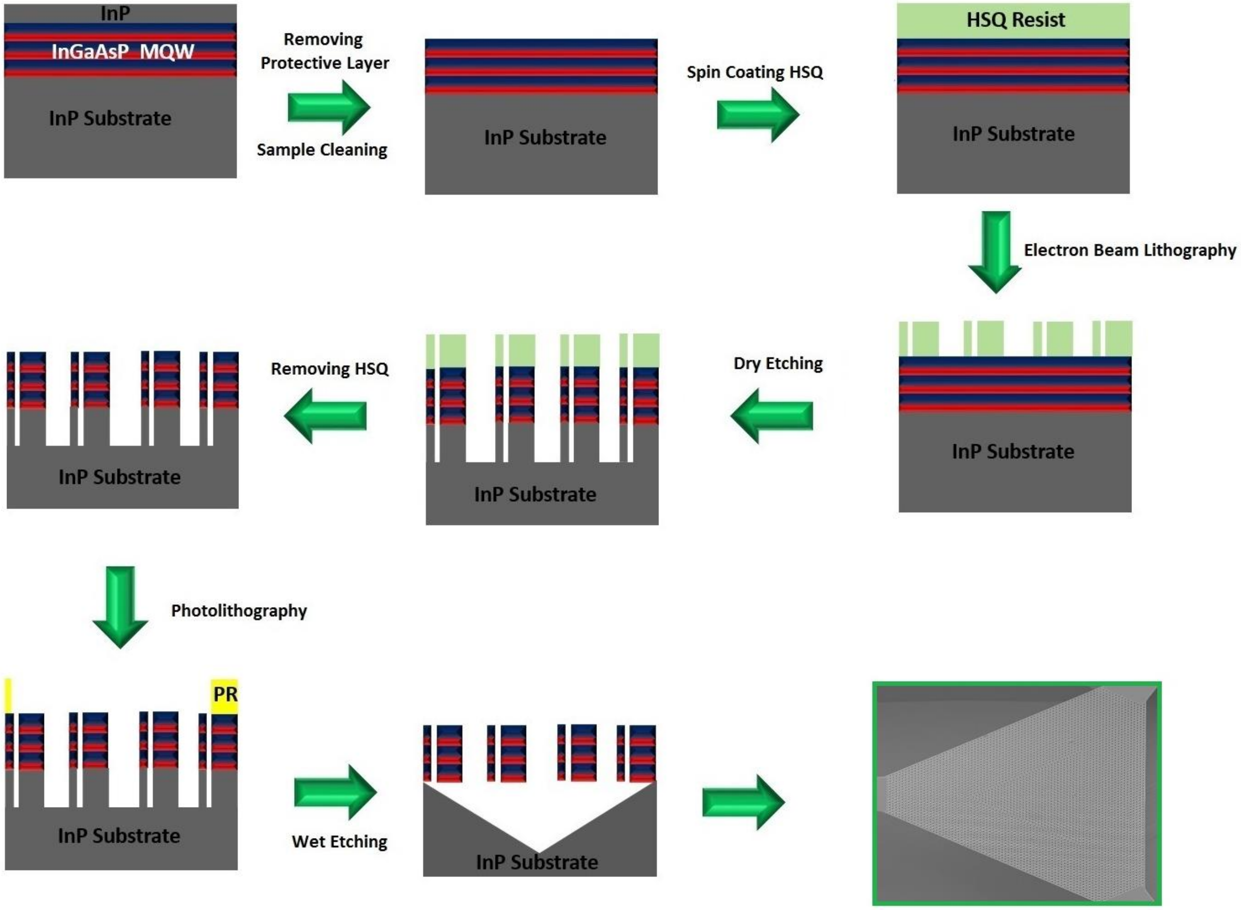

**Fig. 5.** Flowchart of fabrication procedure of suspended valley-Hall photonic crystals.

One of the main reasons we chose a thinner membrane (120 nm) than microdisk slabs was to find the optimal dry etching time more easily. Fig. 6 shows the top-view SEM images of fabricated valley-Hall cavities with increasing dry etching time. As the wafer is dry-etched longer, the etching quality degrades. Specifically, the sidewall profile becomes less vertical, and rather conical shape as the resist is not a perfect step-like profile. However, if the dry etching is not enough, full suspension of a large ($> 36a$) membrane is not guaranteed[31]. Therefore, the dry etching time should be optimized to meet the requirement of both suspension and acceptable sidewall quality, which makes a trade-off relation. In fabricating our valley-Hall cavity, an etching depth of 1 μm with an ICP etching time of 75s was used to achieve it. Fig. 7 shows a high quality fabrication of a valley-Hall cavity with a vertical sidewall in a tilted scanning electron micrograph. The inset presents a magnified image of the bottom-left corner of the triangular cavity and the proximity of small holes at the interface as well as the quality of nanofabrication can be seen.

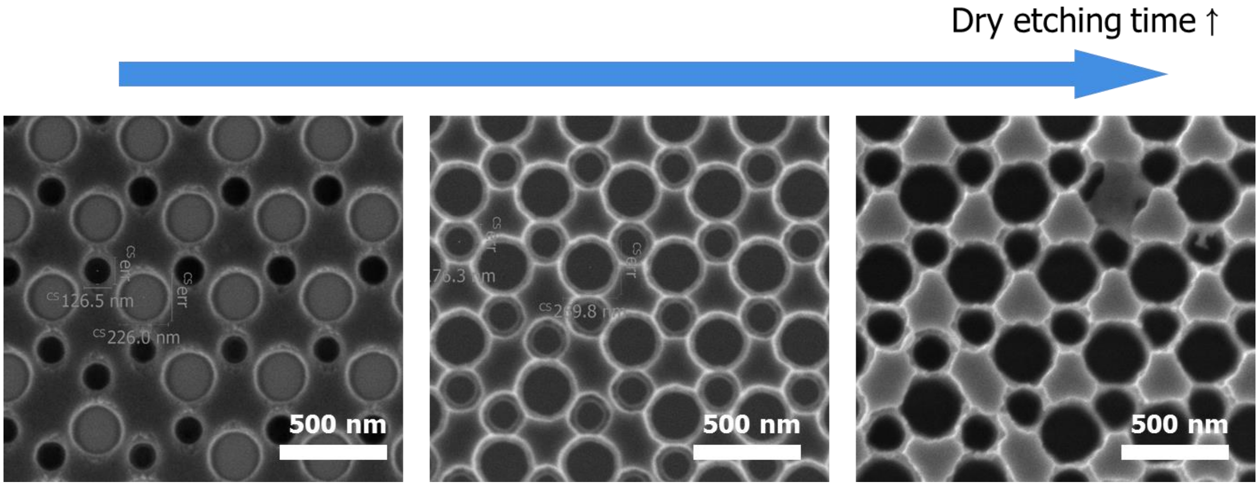

**Fig. 6.** Top-view SEM images of suspended valley-Hall photonic crystals with increasing dry etching time.

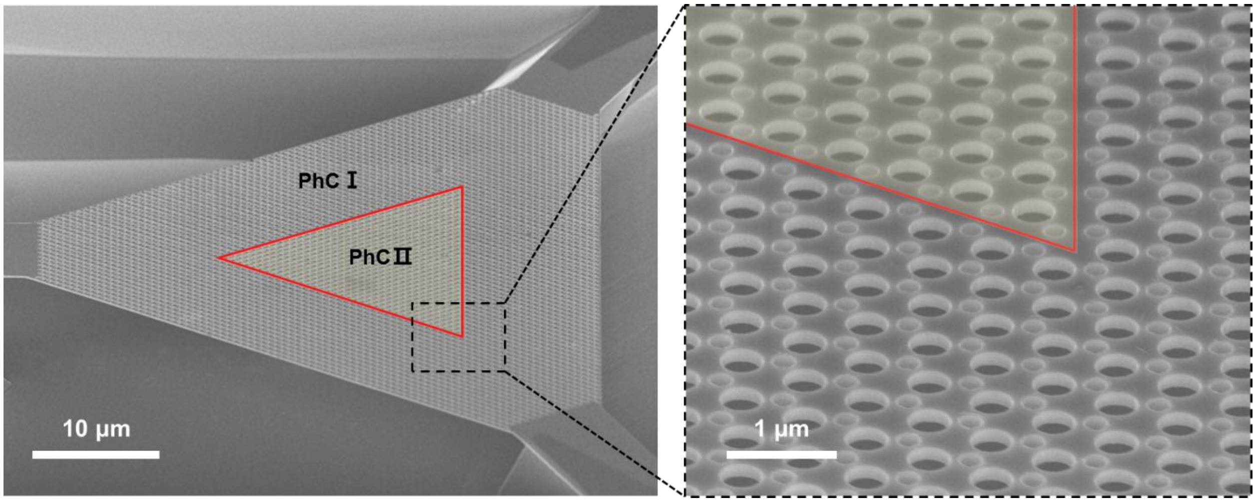

**Fig. 7.** Tilted SEM images of the cavity indicated as a red triangle. The inset presents a magnified image around the bottom-left corner of the triangle where the proximity of small holes at the interface is apparent.

The fabricated valley-Hall cavity is then optically pumped by illuminating the entire surface of the cavity with a laser using a long working distance microscope objective that simultaneously pumps and collects light from the structure. The measurement setup is presented in Fig. 8. The sample is optically pumped from the top side with a 1064 nm pulsed laser (12 ns of pulse width and repetition rate of 215 kHz). A 20x long working distance microscope objective (NA of 0.4) focuses the pump beam on the sample and collects the lasing emission simultaneously. The pump beam size is adjusted by a telescope (lenses $L_1$ and $L_2$) tuning the divergence of the beam. The pump power is finely tuned by an optical attenuator and monitored by a power meter. PL signals are captured by an IR-CCD (Indigo Alpha NIR) and a monochromator (CVI Digikrom DK480) via double 4-f imaging systems. The spectrum is obtained in conjunction with a cooled InGaAs detector in a lock-in detection configuration.

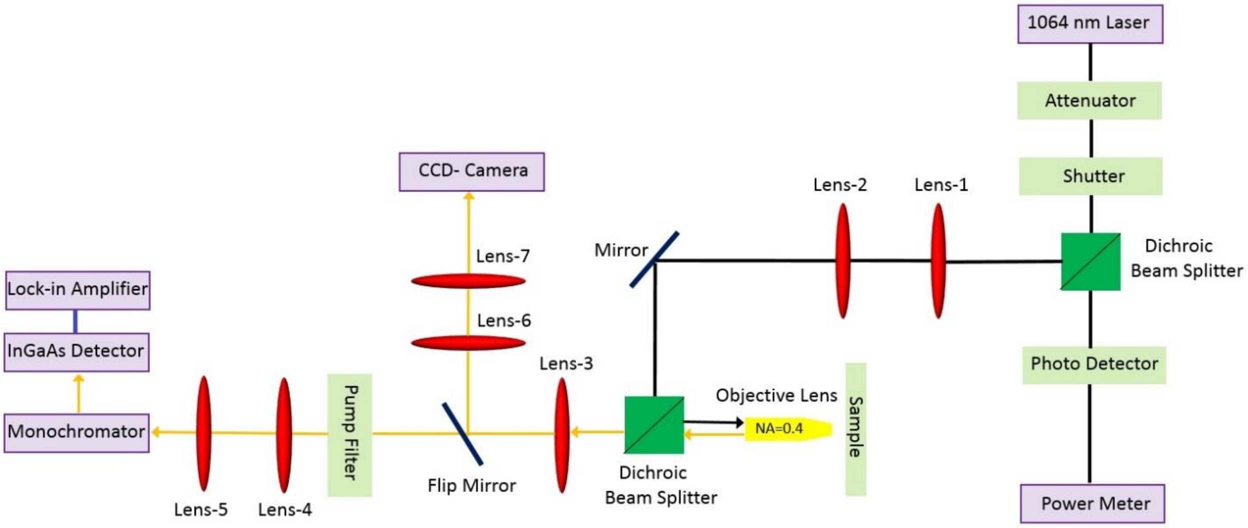

**Fig. 8**. Micro-photoluminescence setup for characterizing valley-Hall topological lasers.

Using the micro PL measurement setup, we first obtained the light-light (*L*-*L*) characteristics of the valley-Hall triangular cavity as shown in Fig 9a. The plot clearly shows a threshold behavior characteristic of lasing. The evolution of the photoluminescence spectrum as a function of the input power density is presented in Fig. 9b. Below the threshold, we observe spontaneous emission. As the pump power is increased, one of the RLM modes starts lasing. The emission from the cavity, captured by a near-infrared charge-coupled device (CCD) under different pump powers, is shown in Fig. 9c. Point 1 in Fig. 9c corresponds to spontaneous emission over a broad area coinciding with the pumping beam pattern. Point 2 corresponds to a dominant spontaneous emission along the perimeter of the triangular cavity. Above threshold (points 3 and 4), lasing occurs, and bright emission is observed only from the vertices of the triangle, in perfect agreement with the expected far-field of the highest quality factor RLM below the light-cone shown in Fig. 4c. We also observe interference fringes between waves scattered at the three vertices, an additional indication of the coherence of the laser.

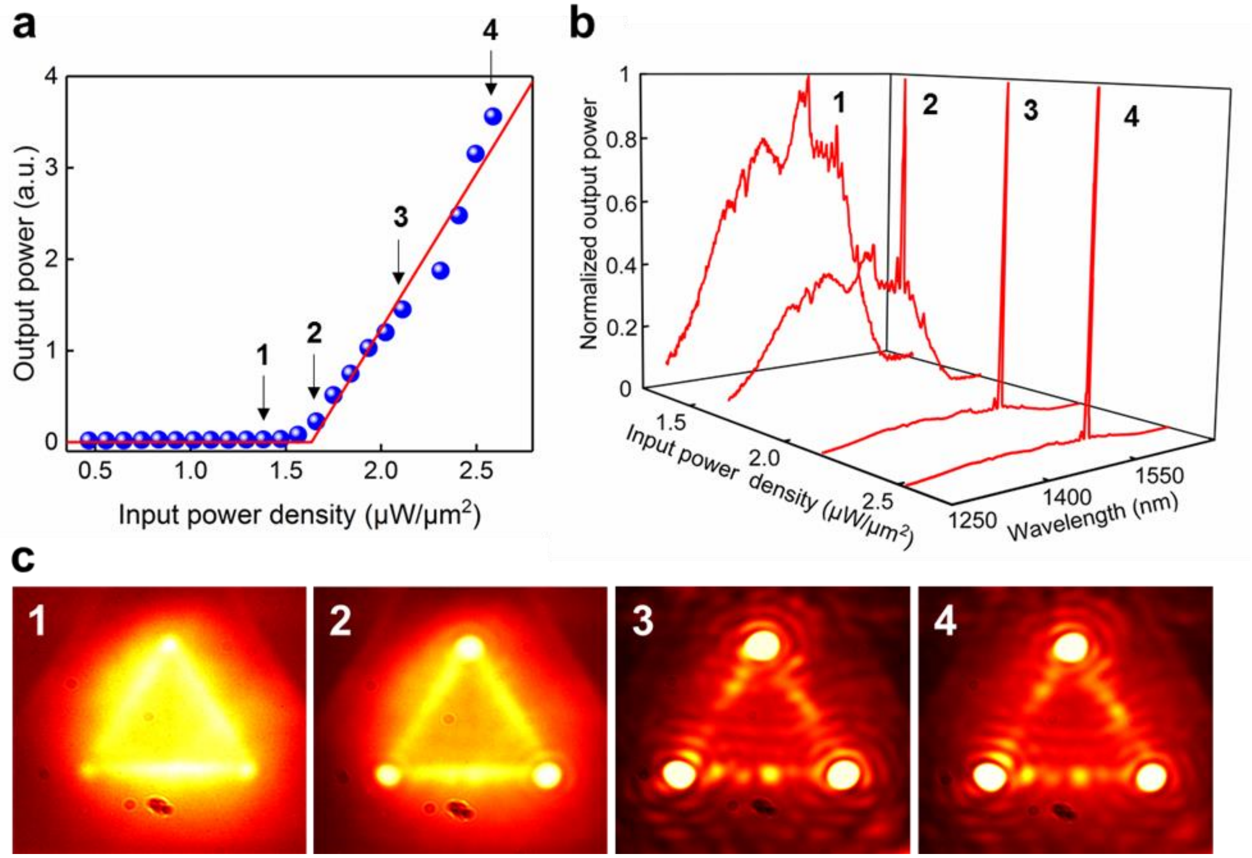

**Fig. 9.** Single-mode topological valley-Hall lasing. **a**, Light-light (L-L) characteristics of a valley-Hall triangular cavity uniformly pumped from the top showing a threshold behavior characteristic of lasing. **b**, Evolution of the photoluminescence spectrum as a function of the input power density. Below threshold, we observe spontaneous emission of ring-like modes (RLMs) with a wavelength spacing of about 10 nm in good agreement with three-dimensional modeling of the cavity. As the pump power is increased, one of the RLM modes starts lasing. **c**, Emission from the cavity captured by a near-infrared charge-coupled device (CCD) under different pump powers. In 1, spontaneous emission over a broad area corresponding to the pumping beam is observed. In 2, spontaneous emission along the perimeter of the triangular cavity is dominant. Above threshold (3 and 4), lasing occurs from a RLM below light-cone, and the side of the triangle is decoupled from radiation with bright emission visible only from the vertices of the triangle, in good agreement with Fig. 4c (bottom).

In addition, we conducted additional experiments to prove our lasing mode is indeed from RLM because our cavity contains a large number of high quality factor modes. First, the emission spectrum below the threshold shows that RLMs with a wavelength spacing of about 10 nm are visible in good agreement with the three-dimensional modeling of the cavity as shown in Fig. 10.

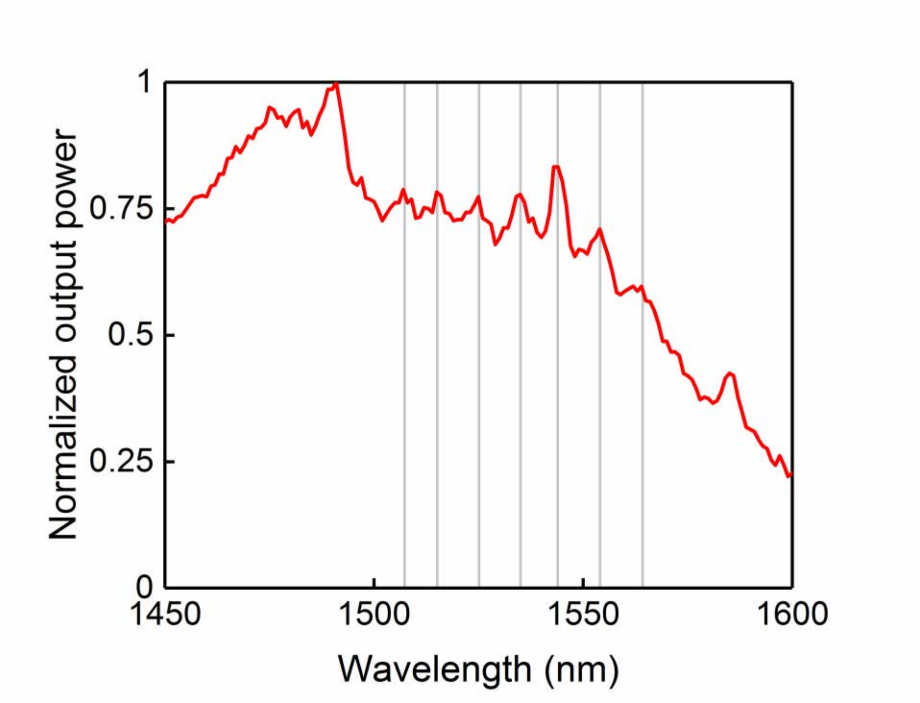

**Fig. 10.** Measured photoluminescence spectrum of a valley-Hall cavity before threshold. Vertical gray lines correspond to local peaks regularly spaced around lasing wavelength.

As another proof of the coherence of our laser, emission spectra from a valley-Hall cavity were also measured when the light is collected from all three corners (blue), two corners (yellow), and only one corner (orange) in Fig. 11. A pinhole aligned with emitted light was used to block the light from the corner(s). As seen in the spectra, all measurements agree well and this implies coherence of the light source.

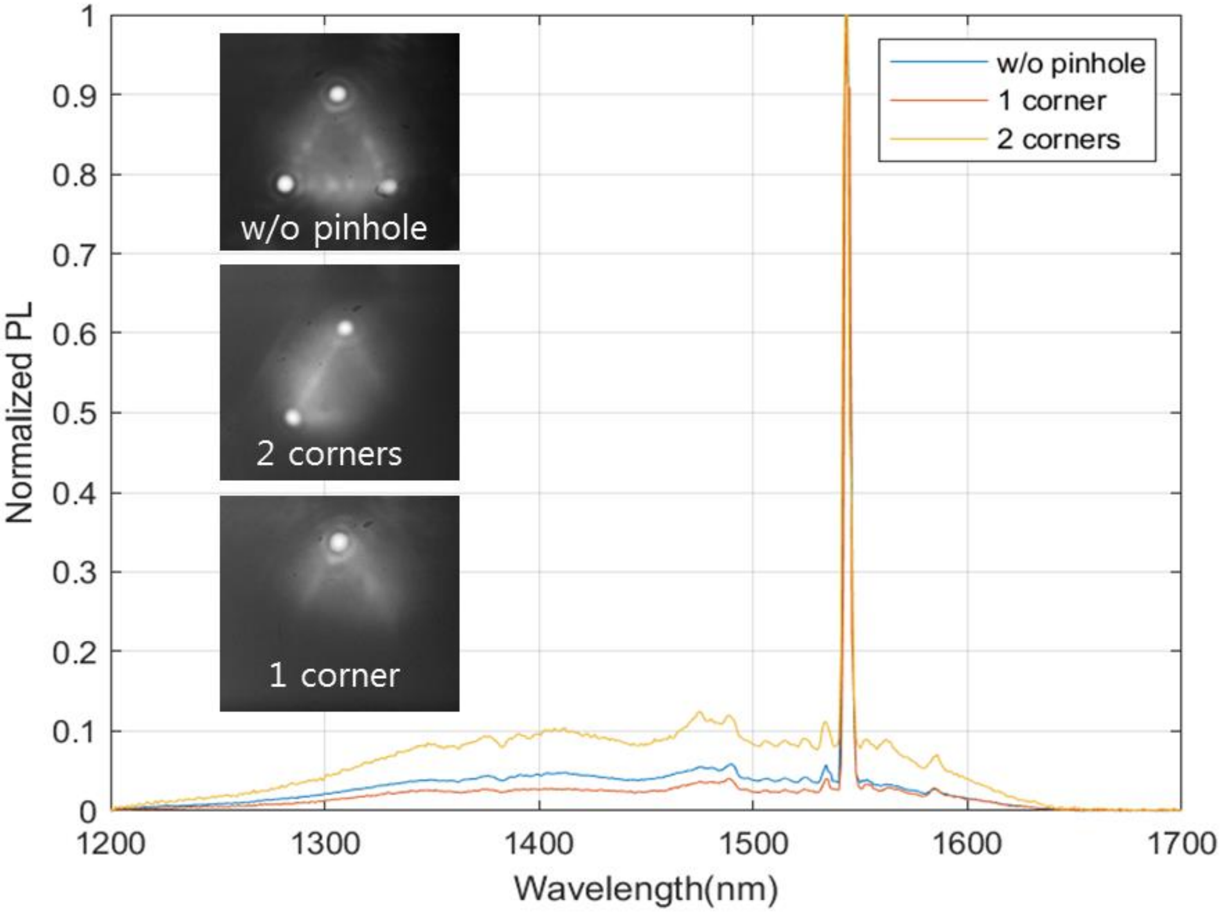

**Fig. 11.** Measured photoluminescence spectrum of emitted light from three corners (blue), two corners (yellow), and one corner (orange). Agreement of three spectra agree implies coherence of our laser.

We have thus demonstrated a single-mode valley-Hall topological ring laser at telecommunication frequency. The cavity, a triangular interface between two honeycomb lattices with opposite valley-Chern numbers, supports edge states confined at the boundary of the photonic crystals with four guiding regimes controlled by the degree of asymmetry of the crystals. The degree of asymmetry, the contrast between the radius of large and small holes in the honeycomb lattice with broken inversion symmetry, governs light confinement in the valley-Hall cavity and enables systematic single-mode operation despite the presence of multiple cavity modes in the topological bandgap. In addition, we identified and categorized existing cavity modes in our valley-Hall cavity into four types, and observed ring-like modes below the light line are the highest quality factor modes for lasing. The ability to simultaneously control the topological phase and the lifetime of photons will enable a new class of linear and non-linear classical and quantum topological optoelectronic devices and systems.

# References

1. J. W. Goodman, F. J. Leonberger, S.-Y. Kung, R. A. Athale, Optical interconnections for VLSI systems. *Proc. IEEE* **72**, 850-866 (1984).
2. P. Cheben, R. Halir, J. H. Schmid, H. A. Atwater, D. R. Smith, Subwavelength integrated photonics. *Nature* **560**, 565-572 (2018).
3. A. Rycerz, J. Tworzydło, C. W. J. Beenakker, Valley filter and valley valve in graphene. *Nat. Phys.* **3**, 172-175 (2007).
4. D. Xiao, W. Yao, Q. Niu, Valley-contrasting physics in graphene: magnetic moment and topological transport. *Phys. Rev. Lett.* **99**, 236809 (2007).
5. W. Yao, D. Xiao, Q. Niu, Valley-dependent optoelectronics from inversion symmetry breaking. *Phys. Rev. B.* **77**, 235406 (2008).
6. T. Ma, G. Shvets, All-Si valley-Hall photonic topological insulator. *New J. Phys.* **18**, 025012 (2016).
7. F. D. M. Haldane, S. Raghu, Possible realization of directional optical waveguides in photonic crystals with broken time-reversal symmetry. *Phys. Rev. Lett.* **100**, 013904 (2008).
8. Z. Wang, Y. Chong, J. D. Joannopoulos, M. Soljačić, Observation of unidirectional backscattering-immune topological electromagnetic states. *Nature* **461**, 772-775 (2009).
9. T. Ozawa, H. M. Price, A. Amo, N. Goldman, M. Hafezi, L. Lu, M. C. Rechtsman, D. Schuster, J. Simon, O. Zilberberg, I. Carusotto, Topological photonics. *Rev. Mod. Phys.* **91**, 015006 (2019).
10. R. O. Umucalılar, I. Carusotto, Artificial gauge field for photons in coupled cavity arrays. *Phys. Rev. A.* **84**, 043804 (2011).
11. M. Hafezi, E. A. Demler, M. D. Lukin, J. M. Taylor, Robust optical delay lines with topological protection. *Nat. Phys.* **7**, 907-912 (2011).
12. M. Hafezi, S. Mittal, J. Fan, A. Migdall, J. M. Taylor, Imaging topological edge states in silicon photonics. *Nat. Photonics* **7**, 1001-1005 (2013).
13. M. C. Rechtsman, J. M. Zeuner, Y. Plotnik, Y. Lumer, D. Podolsky, F. Dreisow, S. Nolte, M. Segev, A. Szameit, Photonic Floquet topological insulators. *Nature* **496**, 196-200 (2013).
14. A. B. Khanikaev, S. Hossein Mousavi, W.-K. Tse, M. Kargarian, A. H. MacDonald, G. Shvets, Photonic topological insulators. *Nat. Mater.* **12**, 233-239 (2013).
15. W. Gao, M. Lawrence, B. Yang, F. Liu, F. Fang, B. Béri, J. Li, S. Zhang, Topological photonic phase in chiral hyperbolic metamaterials. *Phys. Rev. Lett.* **114**, 037402 (2015).
16. Y. Kang, X. Ni, X. Cheng, A. B. Khanikaev, A. Z. Genack, Pseudo-spin-valley coupled edge states in a photonic topological insulator. *Nat. Commun.* **9**, 3029 (2018).
17. M. I. Shalaev, W. Walasik, A. Tsukernik, Y. Xu, N. M. Litchinitser, Robust topologically protected transport in photonic crystals at telecommunication wavelengths. *Nat. Nanotechnol.* **14**, 31-34 (2019).
18. M. A. Gorlach, X. Ni, D. A. Smirnova, D. Korobkin, D. Zhirihin, A. P. Slobozhanyuk, P. A. Belov, A. Alù & A. B. Khanikaev . Far-field probing of leaky topological states in all dielectric metasurfaces. *Nat. Commun.* **9**, 909 (2018).

19. D. D. Solnyshkov, A. V. Nalitov, and G. Malpuech, Kibble-Zurek mechanism in topologically nontrivial zigzag chains of polariton micropillars. *Phys. Rev. Lett.* **116**, 046402 (2016).
20. Y. Ota, K. Takata, T. Ozawa, A. Amo, Z. Jia, B. Kante, M. Notomi, Y. Arakawa, and S. Iwamoto, Active topological photonics. *Nanophotonics* **9**, 547 (2020).
21. P. St-Jean, V. Goblot, E. Galopin, A. Lemaître, T. Ozawa, L. Le Gratiet, I. Sagnes, J. Bloch, A. Amo, Lasing in topological edge states of a one-dimensional lattice. *Nat. Photonics* **11**, 651-656 (2017).
22. M. Seclì, M. Capone, I. Carusotto, Theory of chiral edge state lasing in a two-dimensional topological system. *Phys. Rev. Research* **1**, 033148 (2019).
23. B. Bahari, A. Ndao, F. Vallini, A. E. Amili, Y. Fainman, B. Kanté, Nonreciprocal lasing in topological cavities of arbitrary geometries. *Science* **358**, 636–640 (2017).
24. M. A. Bandres, S. Wittek, G. Harari, M. Parto, J. Ren, M. Segev, D. N. Christodoulides, and M. Khajavikhan, Topological insulator laser: Experiments. *Science* **359**, eaar4005 (2018).
25. S. Mittal, E. A. Goldschmidt, M. Hafezi, A topological source of quantum light. *Nature* **561**, 502-506 (2018).
26. S. Klembt, T. H. Harder, O. A. Egorov, K. Winkler, R. Ge, M. A. Bandres, M. Emmerling, L. Worschech, T. C. H. Liew, M. Segev, C. Schneider, S. Höfling, Exciton-polariton topological insulator. *Nature* **562**, 552-556 (2018).
27. Z. A. Kudyshev, A. V. Kildishev, A. Boltasseva, V. M. Shalaev, Tuning topology of photonic systems with transparent conducting oxides. *ACS Photonics* **6**, 1922-1930 (2019).
28. S. Kruk, A. Poddubny, D. Smirnova, L. Wang, A. Slobozhanyuk, A. Shorokhov, I. Kravchenko, B. Luther-Davies, Y. Kivshar, Nonlinear light generation in topological nanostructures. *Nat. Nanotechnol.* **14**, 126-130 (2019).
29. H. Zhao, X. Qiao, T. Wu, B. Midya, S. Longhi, L. Feng, Non-Hermitian topological light steering. *Science* **365**, 1163-1166 (2019).
30. Y. Zeng, U. Chattopadhyay, B. Zhu, B. Qiang, J. Li, Y. Jin, L. Li, A. G. Davies, E. H. Linfield, B. Zhang, Y. Chong, Q. J. Wang, Electrically pumped topological laser with valley edge modes. *Nature* **578**, 246-250 (2020).
31. W. Noh, M. Dupré, A. Ndao, A. Kodigala, B. Kanté, Self-suspended microdisk lasers with mode selectivity by manipulating the spatial symmetry of whispering gallery modes. *ACS Photonics* **6**, 389 (2019).
32. H.-G. Park, S.-H. Kim, S.-H. Kwon, Y.-G. Ju, J.-K. Yang, J.-H. Baek, S.-B. Kim, Y.-H. Lee, Electrically driven single-cell photonic crystal laser. *Science* **305**, 1444-1447 (2004).
33. Y. Gong, S. Wong, A. J. Bennett, D. L. Huffaker, S. S. Oh, Topological insulator laser using valley-hall photonic crystals. arXiv:2001.03661 (2020).
34. H. Zhong, Y. Li, D. Song, Y. V. Kartashov, Y. Zhang, Y. Zhang, Z. Chen, Topological valley hall edge state lasing. arXiv:1912.13003 (2019).

35 Kodigala, A., Lepetit, T., Gu, Q., Bahari, B., Fainman, Y., Kanté, B. Lasing Action from Photonic Bound States in Continuum. *Nature* **541**, 196–199 (2017).

35 Kodigala, A., Gu, Q., Lepetit, T., Bahari, B., Kanté, B. Mechanically Stable Conjugate

and Suspended Lasing Membranes of Bridged Nano-Cylinders. *Opt. Mater. Express* **7**, 2980–2992 (2017).

# 4

# *Single-Mode Surface-Emitting Photonic Crystal Laser*[*]

## 4.1 Introduction

The scaling of laser cavities, since the invention of lasers, is a long-standing question that has been investigated but has still not been resolved[1-3]. It is limited by the fact that the ode spacing between the fundamental mode (which is often target lasing mode) and the higher order modes fundamentally goes to zero as the length of the cavity increases. This limitation has spurred extensive studies on vertical-cavity surface-emitting laser arrays as well as photonic crystal surface-emitting lasers for single-mode operation[4-10]. In this chapter, we report unconventional cavities exploiting Dirac singularities with linear dispersion, with an emphasis on the experimental side. A more detailed discussion of the theory will be presented in another dissertation paper. Dirac points are topological singularities that have gained enormous interest since the discovery of unique electronic transport in graphene, attracting wide interest from the multidisciplinary areas[11-16]. In photonics, Dirac cones with linear dispersion have mostly been utilized to demonstrate effective zero-index materials[17-24]. For cavities with a quadratic dispersion, strongly detuned from the Dirac singularity, the complex frequencies of modes converge towards each other with the size of cavities, making lasers constructed from such cavities multimode. Interestingly, with linear

---

[*] The following section, in part, has been submitted for journal publication in a similar form. (R. Contractor*, W. Noh*, W. Redjem*, B. Kanté, "Scalable Single-mode Surface Emitting Laser via Open-Dirac Singularities", submitted, 2022)

dispersion, we observed that the normalized complex free-spectral range converges to almost a constant. This unconventional scaling of the complex frequency of modes makes the cavity scale-invariant and enables single-mode lasing operation.

## 4.2 Fabrication of freestanding photonic crystal array membrane

Our proposed structure is presented in Fig. 1a. It is a photonic crystal (PhC) with a hexagonal lattice. The unit-cell of the PhC is presented in the inset of Fig. 1b. As shown in Fig. 1c, our cavity is formed by truncating the PhC as a hexagon around a central air-hole with edges normal to the M-directions of the lattice. The entire cavity is suspended in air, and it is connected to the main membrane by six bridges at the corners of the hexagon for mechanical support.

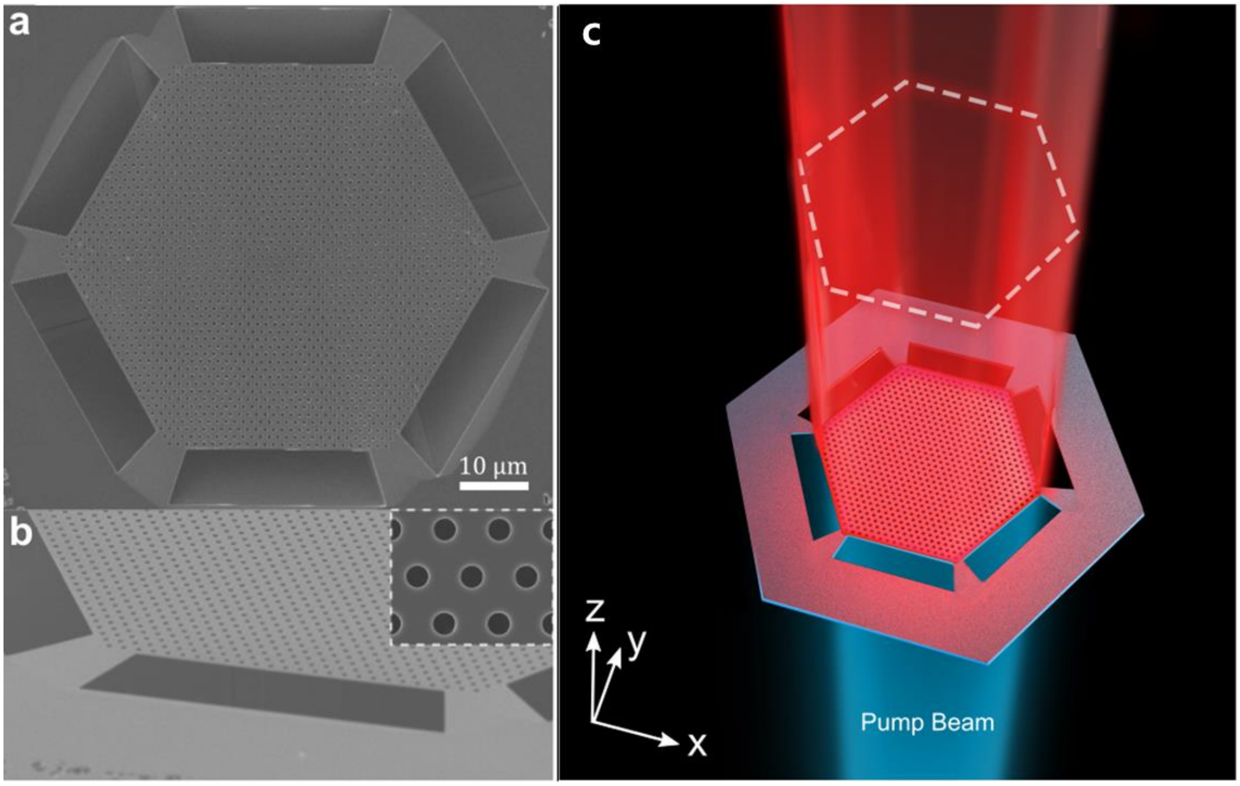

**Fig. 1. a,** Top view scanning electron micrograph of a hexagonal lattice photonic crystal (PhC) that is truncated to form an open-Dirac electromagnetic cavity. The free-standing structure is suspended via six bridges connecting the main membrane to the substrate along the ΓK direction. The cavities are fabricated using electron beam lithography, inductively coupled plasma etching, and wet etching. **b**, Titled view of the cavity showing two bridges, the array of holes, and the PhC-air boundary. The thickness of the membrane is 200 nm, the period of the crystal is 1265 nm, and the radius of holes is used to tune cavities around the Dirac singularity. The inset shows the quality of the nanofabrication with near-perfect circular air-holes interfaces. **c,** Schematic of a laser illustrating the pump beam (blue) and the lasing beam (red) from a cavity mode.

To confirm the scalable single-mode photonic crystal cavity, it is preferred to fabricate the largest array possible. Compared to the previous fabrication of microdisks and valley-Hall cavities, this fabrication requires sophisticated modifications. Fig. 2 illustrates and summarizes the flowchart of the overall nanofabrication process. The photonic crystal cavity is prepared on 200 nm InGaAsP multiple quantum wells (MQWs) with a gain spectrum over telecommunication wavelength at 1550 nm. Note that the wells and barriers repeat six times. After the InP capping layer is removed, the InGaAsP wafer is cleaned by typical acetone and isopropyl alcohol ultrasonication for 10 min each. Subsequently, hydrogen silsesquioxane (HSQ) negative tone resist, with its advantage of great selectivity against inductively coupled plasma (ICP), is spin-coated on the wafer, and the photonic crystal is patterned by electron-beam lithography (Fig. 2a). To avoid unwanted wet etching of the InP sacrificial layer, we added photolithography (Fig. 2b). In the following step, ICP dry etching with a mixture of $H_2$, $CH_4$, Ar, and $Cl_2$ gas is performed to transfer the patterns to the InGaAsP slab. Then the HSQ layer is removed by a buffered oxide etchant (BOE) solution (Fig. 2c). The device is suspended by a diluted HCl (3:1) solution which selectively removes the InP sacrificial layer under the InGaAsP (Fig. 2d). To suspend a large area membrane, we introduced the critical point drying (CPD) technique (Fig. 2e). IPA was used as an exchanging solvent, and the supercritical phase of carbon dioxide ($CO_2$) is obtained at the pressure of 1350 psi and a temperature of 31°C. The sample is finalized after supercritical phase carbon dioxide drying (Fig. 2f).

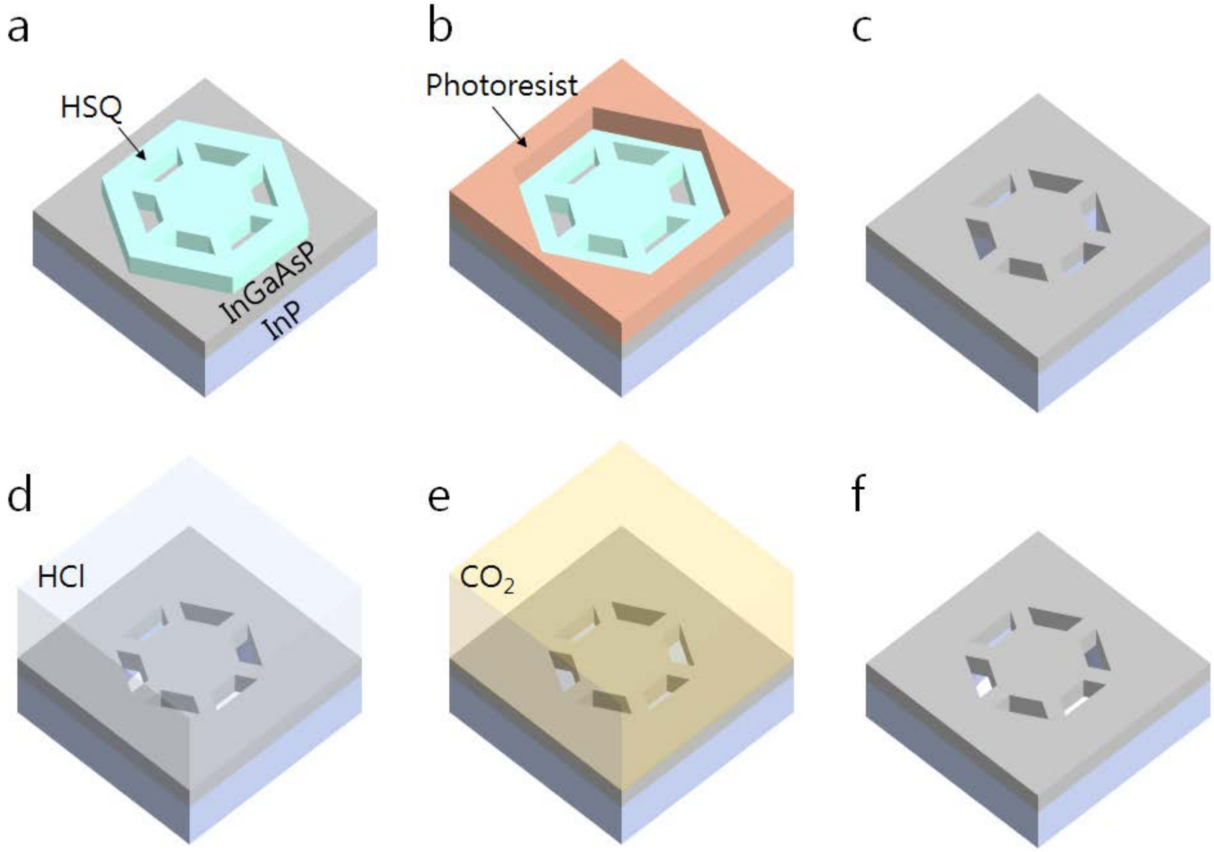

**Fig. 2.** Summary of fabrication steps for a large-scale suspended Dirac photonic crystal cavity. **a**, Electron-beam lithography to define photonic crystal. **b**, Photolithography to protect sacrificial InP layer. **c**, Dry etching and resist removal. **d**, Wet etching of InP sacrificial layer under the photonic crystal slab using HCl solution. **e**, Critical point drying method to avoid stiction of suspended slab. **f**, Suspended photonic crystal slab.

There were noteworthy changes to enable freestanding large-scale photonic crystal array fabrication. First, compared to previous fabrications steps used in microdisks and valley-Hall cavities, we switched the order of steps, moving ICP dry etching step right after the additional photolithography to protect the sacrificial InP layer elsewhere than the photonic crystal area during the wet etching. This allows a longer wet etching process enough to suspend a large-scale slab completely. Second, we introduced the CPD process, which is commonly used in MEMS fabrication, to avoid stiction issues induced by the capillary force when drying the sample. Especially for devices larger than 35 unit-cells, it is critical to eliminate surface tension associated with the drying of a liquid by avoiding the phase transition boundary from liquid to gas. Finally, we optimized writing conditions such as electron beam dose and proximity effect correction (PEC) parameters so that uniform geometry along the large cavity is maintained.

To elaborate on the latter, the proximity effect is due to the unwanted energy deposition from electron scattering in the resist. In general, this effect becomes more severe as the area increases and as the beam exposure becomes more crowded. It can be characterized as a point spread function, which is known as a superposition of two Gaussian functions. To calculate electron scattering, we used TRACER (GenISys GmbH) software to conduct a Monte-Carlo method. In the simulation, one million electrons are excited on the resist on the top of the InP substrate to be consistent with the layers used in fabrication. The calculated trajectories of electrons are presented in Fig. 3a. These calculated results can be transferred to the point spread function (Fig. 3b), and then to the dose distribution profile automatically produced with proximity correction based on the function using BEAMER (GenISys GmbH). Note that the center area has the smaller dose, while the corner area has the larger dose, and this is because the crowded area has more electrons scattered from the neighboring areas. Using the strategies proposed for the large-scale fabrication, we could successfully suspend 51 unit-cells cavities without any defect (Fig. 3d). Note that the smoothness of air holes, as well as uniformity, is implemented well (Fig. 3e). As shown in Fig. 3f, however, most of the 101 unit-cell cavities have critical cracks possibly induced either by the weight of the suspended slab or by the volatile wet etching process.

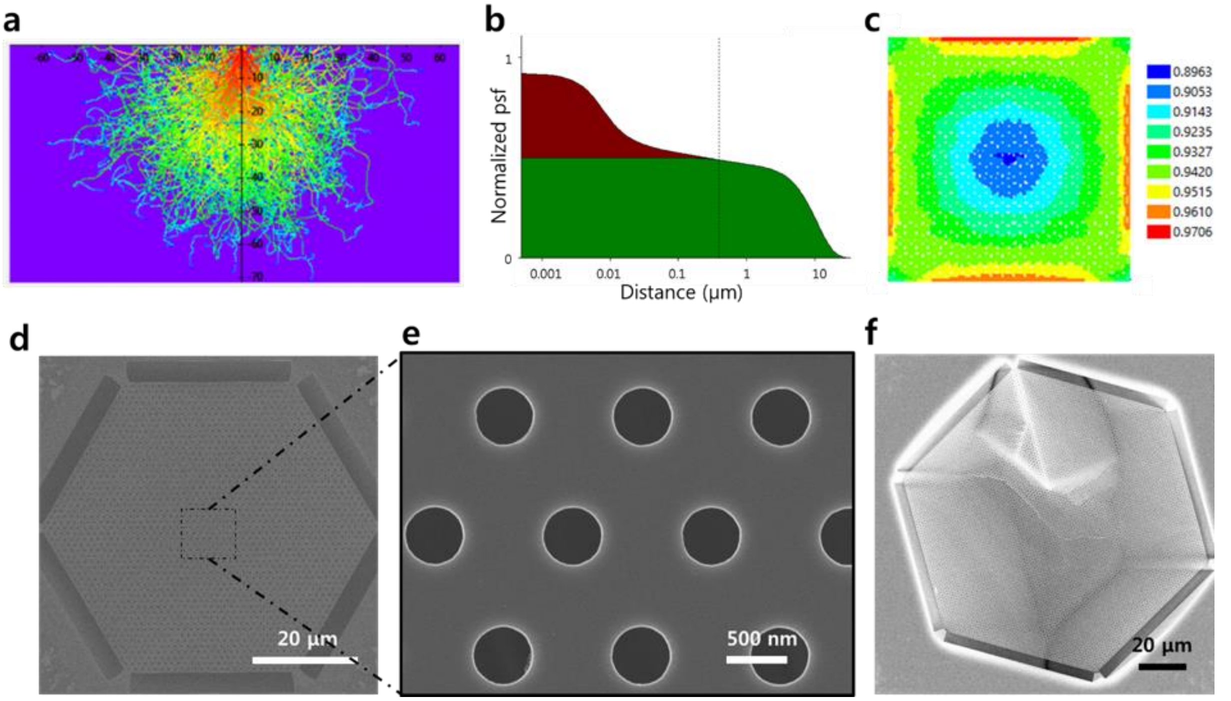

**Fig. 3.** **a**, Calculated scattering trajectories of 1,000,000 electrons by Monte-Carlo simulation. **b**, Normalized point spread function calculated from **a**. **c**, Relative dose distribution along with the photonic crystal array. **d**, Scanning electron micrograph (SEM) of a 51 unit-cells array and **e**, magnified view showing triangular unit-cell with a circular air hole. **f**, SEM image of 101 unit-cell arrays showing a crack at the center.

While most devices were successfully suspended up to 51 unit-cells, larger size cavity showed a low yield to be suspended without any defect or crack mostly due to the lack of mechanical support. Suspension often failed in the wet etching step to relieve the sacrificial InP layer. To investigate suspending mechanism and strategy to improve yield, we fabricated 81 unit-cells photonic crystal arrays with different bridge dimensions (Fig. 4.a and b). We chose the bridge length $L$ and width $w$ to be 6, 12 μm, and 1.7, 3, 5, and 7 μm, respectively. A total of 15 devices were fabricated for each configuration. Most broken membranes have at least two disconnected bridges from the frame due to insufficient support. When disconnected from the frame, the crack is often observed in the thin InGaAsP membrane. There are two possibilities to explain this: the impact is applied to thin InGaAsP slabs when the bridges are broken, or survived bridges couldn't support due to the weight of suspended slabs when drying wet etchant. Fig. 4d represents the most observed suspension failure having disconnections at the three bottom corners (red circles), and the crack formed near the broken bridges (dark blue square). We added the critical point drying method to minimize this, but the suspension yield was still poor (< 20%) when the size of the cavity is large (> 81 unit-cells).

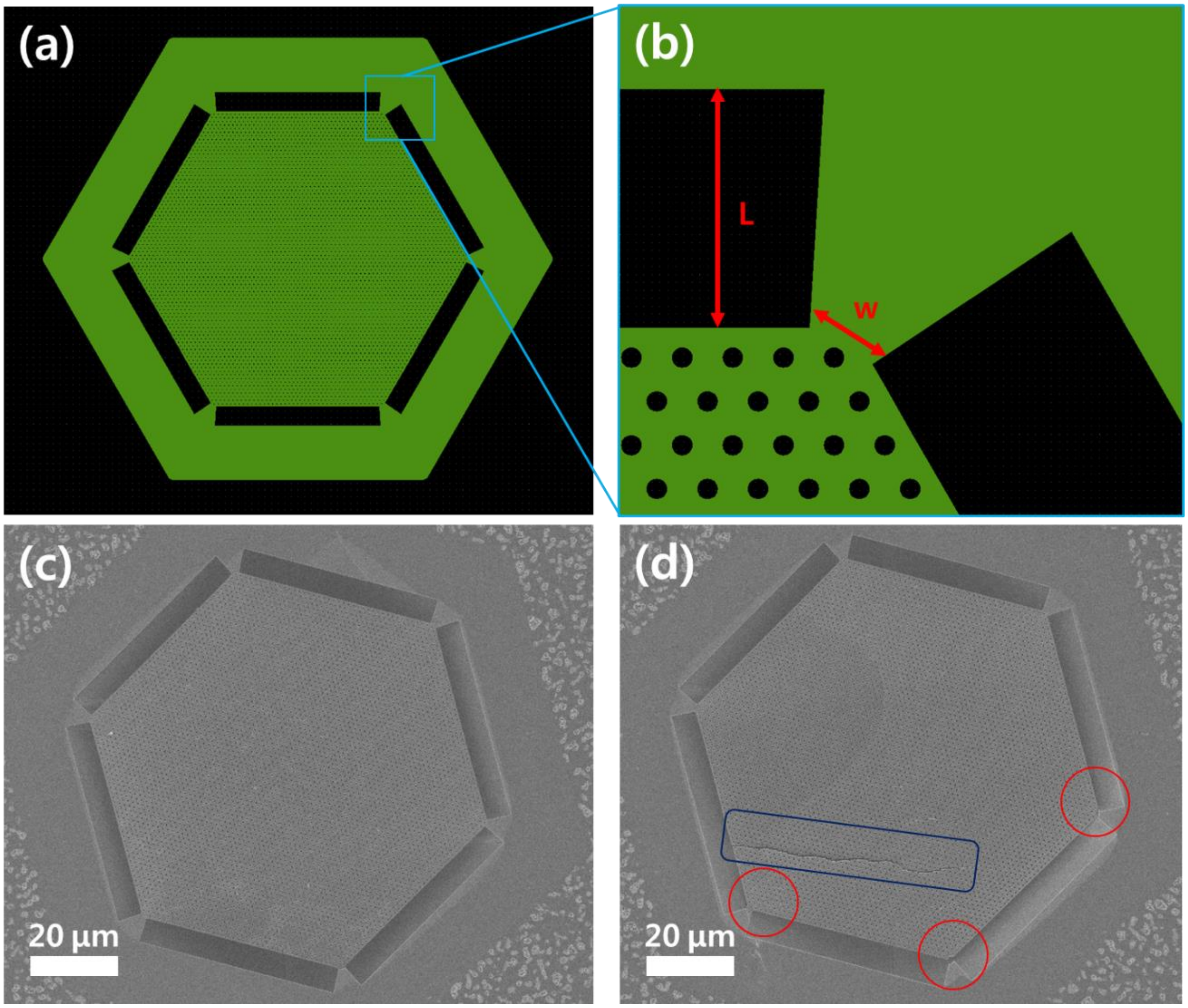

**Fig. 4. a**, Mask pattern of zero-index photonic crystal array (81 unit-cells) used in electron beam writing. **b**, Magnified view of near a corner hexagonal cavity connected to frame with a bridge (L: length of the bridge, w: width of the bridge). The scanning electron micrograph of a successfully suspended (**c**) and a cracked zero-index cavity (**d**). Three red circles denote disconnected bridges and the dark blue square represents the crack formed during the wet etching. Note that devices in (**c**) and (**d**) have the same dimension of L (6 μm) and w (1.7 μm) as well as size (81 unit-cells).

Table 1 summarizes the suspension yield of the fabricated photonic crystal array of 81 unit-cells. To limit our discussion on suspension, we counted devices without any defect or crack before wet etching, and it is why the total numbers are smaller than 15. We could observe that the yield is higher as both $L$ and $w$ increase from this result. The highest yield of ~ 70% was achieved in the case of the thickest and longest bridges ($L$=12 μm, $w$=7 μm). It is expected for width to have this trend because thicker bridges give more mechanical support to the photonic crystal array. On the other hand, in the same manner, we expected a higher yield for shorter bridges as longer bridges can give less mechanical support. However, the result shows significant improvement in yield when the bridges are twice longer. This can be explained by the advantage of longer bridges and larger trench openings. When the opening is too small, removed InP material by the HCl wet etchant can pass the opening too fast and it can make the wet etching process more violent. This can form unwanted vibration and result in disconnection and cracks in the InGaAsP membrane. This contradictory result suggests a trade-off relation between stronger mechanical support and a larger trench.

| Width (*w*) | Length (*L*) | Yield | Width (*w*) | Length (*L*) | Yield |
|---|---|---|---|---|---|
| 1.7 μm | 6 μm | 2/12 (16.7%) | 1.7 μm | 12 μm | 1/14 (7.1%) |
| 3 μm | 6 μm | 1/8 (12.5%) | 3 μm | 12 μm | 6/12 (50%) |
| 5 μm | 6 μm | 2/5 (40%) | 5 μm | 12 μm | 6/14 (42.9%) |
| 7 μm | 6 μm | 1/4 (25%) | 7 μm | 12 μm | 9/13 (69.2%) |

**Table 1.** Summary of suspension yield of devices with different widths (*w*) and lengths (*L*).

The most important factor determining lasing mode behavior in our system is the uniformity of the photonic crystal array, that is the radii of the hole in a hexagonal unit-cell. The proximity effect is one of the main challenges when writing large-scale photonic devices. Although this can be improved by applying PEC offered by an electron beam lithography software as discussed, we also investigated the uniformity of radii in a photonic crystal array in a quantitative manner as well as the limit in the current method and propose alternative solutions. To quantify the proximity effect, we measured the radii of inverted holes along a diagonal of the hexagonal cavities by using an automated feature size measurement tool (GenISys proSEM). As shown in Fig. 5a and b, which represent the radii profile along the diagonals of 35 and 51 unit-cells devices, respectively, we observed a non-uniformity even after PEC is applied. The radius of inverted holes is smaller in the center than the edge as we are using a negative tone hsq resist. In addition, a larger cavity consistently exhibits more non-uniformity as expected. Fig. 5c and d show the evolution of photoluminescence spectra with input power of 35 and 51 unit-cell devices, respectively, presenting non-uniformity of photonic crystal array determines lasing. The 35 unit-cell device, with a more uniform radii profile, lases as shown in Fig. 5c, while the 51 unit-cell device does not (Fig. 5d). Using the ebeam writer at UCSD (Vistec EBPG 5200) and conventional PEC offered by Beamer, we could observe lasing from devices up to 35 unit-cells.

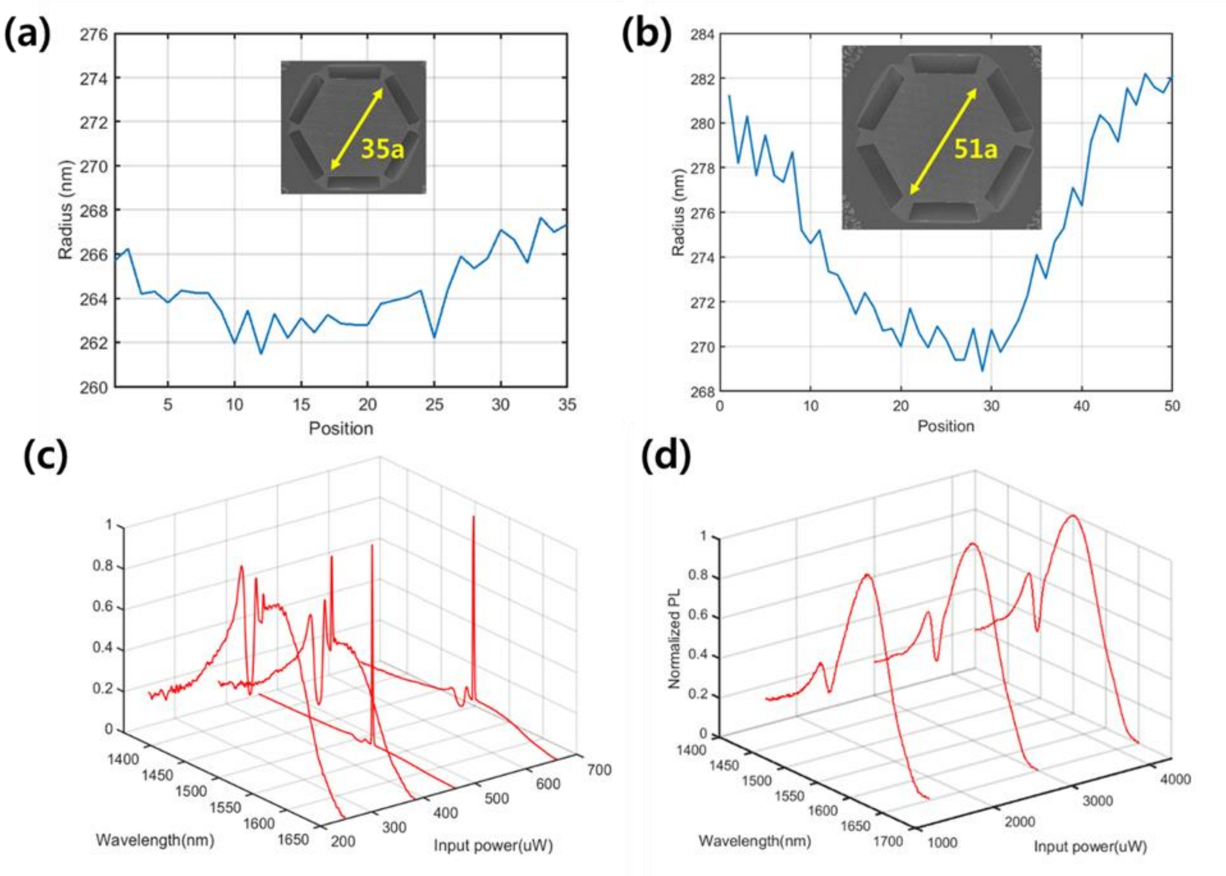

**Fig. 5.** Measured radii profile along a diagonal and the evolution of measured spectra of the hexagonal cavities of (**a, c**) 35 unit-cells and (**b, c**) 51 unit-cells. Insets show SEM images of devices.

There are several ways to minimize the proximity effect. First, it will be beneficial to use positive resist instead of negative tone HSQ resist. In our photonic crystal design, the area of the inverted circle takes only about 1/6 of the hexagonal unit-cell ($R$=273 nm, $a$=1267 nm). As the writing area increases, the backscattered electrons inducing the proximity effect become more. Therefore, switching to positive resist does not only reduce writing time but also reduces the proximity effect. However, this cannot eliminate the issue, and common positive resists such as PMMA or ZEP are generally worse dry etching mask materials than the HSQ. Especially, our process requires good selectivity to achieve full suspension in the following wet etch step. Using multiple masks and transfer processes can solve this problem but it will take a large amount of time to develop the whole new process. Second, it is worth trying the improve PEC. Fig. 6a plots shows the measured radii profile (black circles) of a 51 unit-cell cavity and the parabolic fitting (orange solid line, $R(p) = R_0 + a*p^2$ where $a$=0.027, $R_0$=271 nm). We found that the fitting agrees well with the measurement. To manually compensate for the parabolic non-uniformity, inverted parabolas with *a* value of 0 (red dash line), 0.01(green dash line), 0.025(purple dash line), 0.05 (sky blue dash line) are presented. In Fig. 6b, the GDS layout image of a 51 unit-cell cavity is shown with the unit cell at the center (*R*=263 nm) and the edge (*R*=231 nm) as an example.

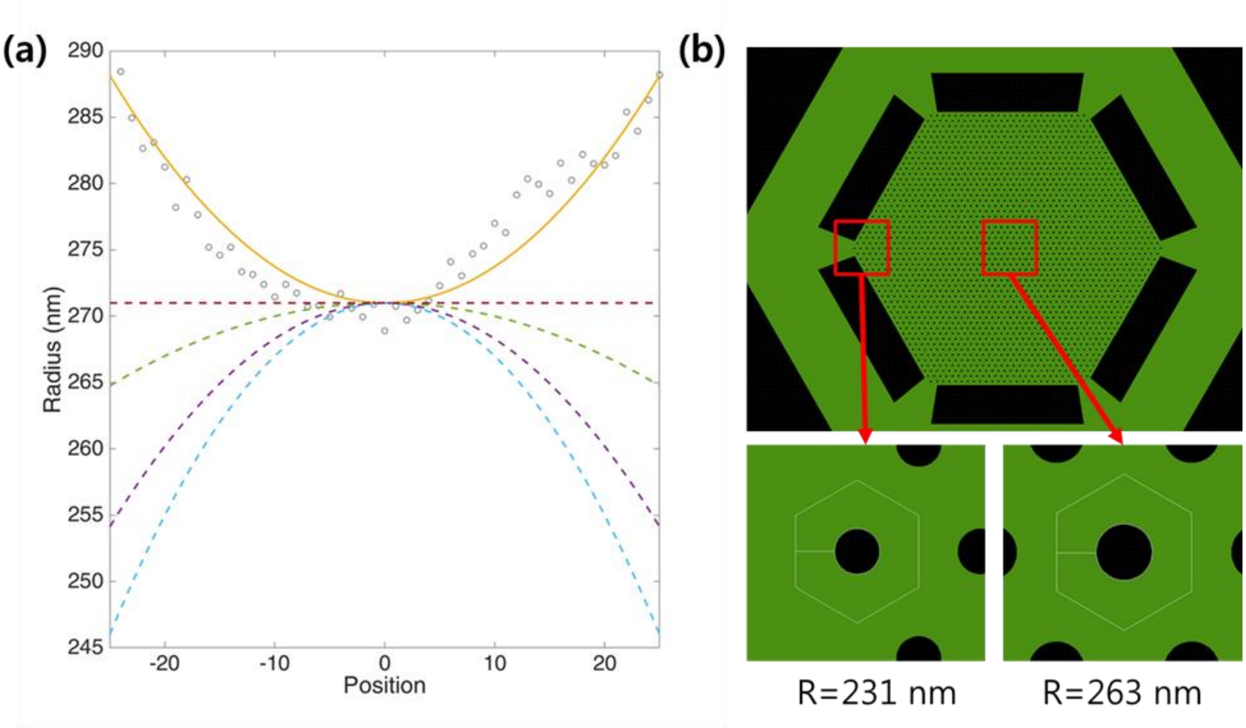

**Fig. 6. a**, Measured radii profile (black circle) of a 51 unit-cell device with a parabolic fitting (orange solid). The inversely compensated parabolic curves with ‘a’ of 0 (red dash line), 0.01 (green dash line), 0.025 (purple dash line), and 0.05 (sky blue dash line). **b**, The image of the GDS layout file of 51 unit-cell cavities with the center radius (R=263 nm) and the edge radius (R=231 nm). The white outline indicates a hexagonal unit-cell.

After a few trials, we found that the best parabolic fitting value is around 0.04. Fig. 7 shows the radii profile of 43 unit-cell devices with different writing conditions. All three have the same nominal radius of 243 nm (note that the actual radius is increased due to lateral extension after dry etching), while blue, orange, and yellow has the parabolic fitting value *a* of 0.05, 0.04, and 0.04 as well as the dose of 450, 475, and 500 μC/cm$^2$, respectively. It is seen that the uniformity is improved compared to PEC using Beamer (see Fig. 5b), and we observed lasing at the target mode from the 43 unit-cells devices for the first time. However, there are still things to improve. For example, from the edge side of the yellow curve (a: 0.04, R: 243nm, dose: 500 μC/cm$^2$), the radius goes up and down twice along the 43 unit-cells, indicating the parabolic fitting we applied is not perfectly compensates the proximity effect. This could be further improved by more trials or the secondary fitting of a given profile. It can also be useful to use the advanced ebeam writer at other facilities such as Molecular Foundry at Lawrence Berkeley Lab.

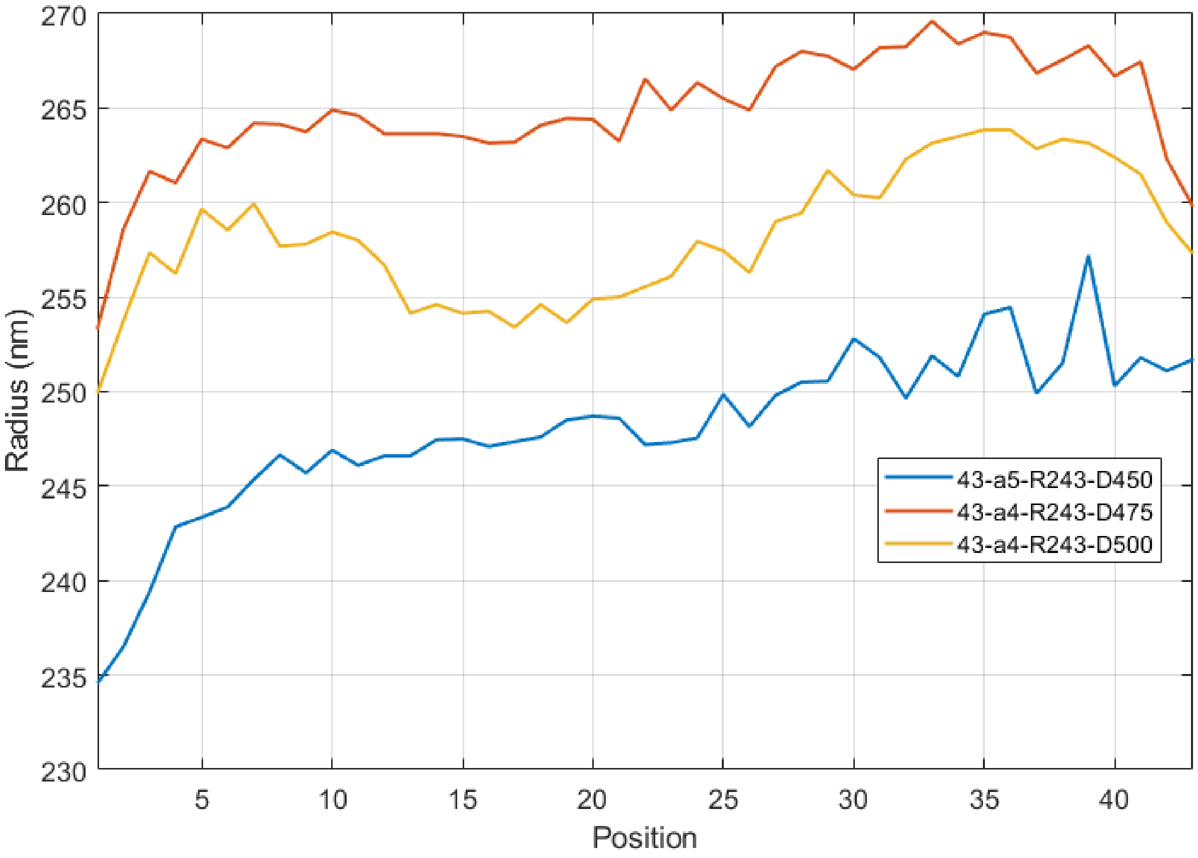

**Fig. 7.** Measured radii profile of 43 unit-cell devices fabricated using the manual parabolic fitting. Blue, orange, and yellow curves are measured from the devices with the parabolic fitting value of 0.05, 0.04, and 0.04, nominal radius of 243 nm for all, and dose of 450, 475, and 500 μC/cm$^2$, respectively.

## 4.3 Experimental demonstration of infinitely scalable photonic crystal laser

Using the fabrication steps discussed in the previous section, we fabricated and characterized our lasers of diameter $D=19a$ (Fig. 8a), $D=27a$ (Fig. 8e), and $D=35a$ (Fig. 8i) to experimentally demonstrate our Dirac cavities. Note that we observed target mode lasing up to $D=43a$ devices using the manual PEC discussed in the previous section, but the result will be included in the other dissertation. Fig. 8 presents the evolution of the normalized output power as a function of the wavelength and the size of the cavity for unit-cell holes radii smaller than the singular radius $r_{\mathrm{Dirac}}$ (Fig. 8b, f, j), equal to $r_{\mathrm{Dirac}}$ (Fig. 8c, g, k), and greater than $r_{\mathrm{Dirac}}$ (Fig. 8d, h, l). For $D=19a$, cavities are single-mode for $r < r_{\mathrm{Dirac}}$ (Fig. 8b), $r = r_{\mathrm{Dirac}}$ (Fig. 8c), and $r > r_{\mathrm{Dirac}}$ (Fig. 8d). For $D=27\mathrm{a}$, cavities remain single mode for $r < r_{\mathrm{Dirac}}$ (Fig. 8f), $r = r_{\mathrm{Dirac}}$ (Fig. 8g), and $r > r_{\mathrm{Dirac}}$ (Fig. 8h). This is because these cavities are relatively small. However, when the size of cavities is increased to $D=35a$ or larger, we observe that they become multimode for $r < r_{\mathrm{Dirac}}$ (Fig. 8j), remain single mode for $r = r_{\mathrm{Dirac}}$ (Fig. 8k), and become multimode for $r > r_{\mathrm{Dirac}}$ (Fig. 8l). The Dirac singularity erases higher-order modes in open-Dirac cavities and lasers remain single-mode when the size is increased. It is worth noting that the uniform field profile across the aperture for the fundamental mode depletes gain across the aperture, making it more difficult for higher-order modes to lase. Single-mode lasing is thus maintained even for near-damage-threshold pump power (see Fig. 9). Our lasers are thus robust to size and pump power density scaling because of the non-vanishing complex free-spectral range and the participation of all unit-cells (or resonators) in the aperture to the lasing mode. These experiments make them the first scale-invariant surface-emitting lasers. It is worth noting that the apparent high threshold power density of our lasers originates from surface recombination since we are directly structuring the quantum wells, and it is comparable to previously reported lasers using a similar strategy[26]. This can be alleviated by designing alternative structures or by additional chemical treatments of the devices. Our cavities are in principle infinitely scalable if the proposed open-Dirac potential can be implemented exactly. In practice, considerations such as proximity effects in lithography, electrical injection, or heat release will need to be addressed for high power devices.

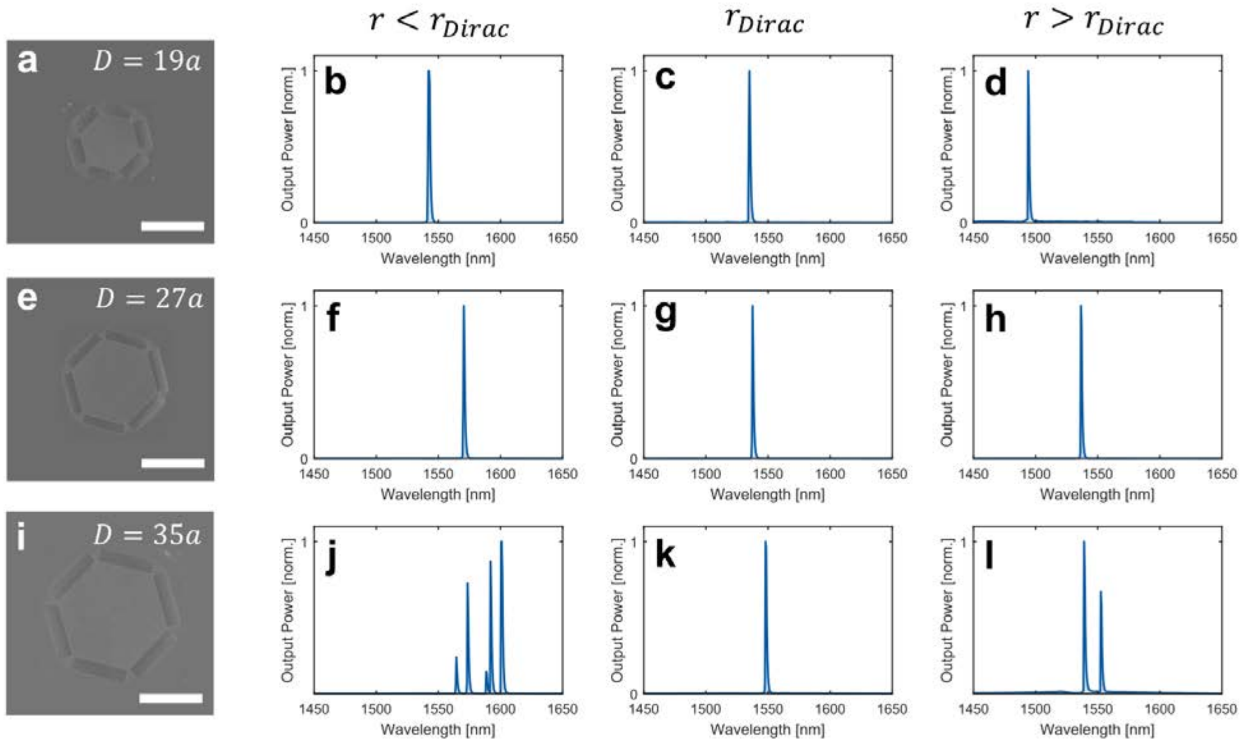

**Fig. 8.** Top-view SEM of fabricated open-Dirac cavities of size $D$=19a (**a**), $D$=27a (**e**), and $D$=35a, where $D$ is the diameter of the aperture and a is the size of the unit-cell of the photonic crystal. The scale bars represent 25μm. Evolution of the normalized output power as a function of the wavelength and the size of the cavity for unit-cell holes radii smaller than the singular radius $\mathrm{r_{Dirac}}$ (**b**, **f**, **j**), equal to $\mathrm{r_{Dirac}}$ (**c**, **g**, **k**), and greater than $\mathrm{r_{Dirac}}$ (**d**, **h**, **l**). The pump power density is 1.1μW/μm$^2$ in all cases. For $D$=19a, cavities are single-mode for $r < r_{\mathrm{Dirac}}$ (**b**), $r = r_{\mathrm{Dirac}}$ (**c**), and $r > r_{\mathrm{Dirac}}$ (**d**). For $D$=27a, cavities are single-mode for $r < r_{\mathrm{Dirac}}$ (**f**), $r = r_{\mathrm{Dirac}}$ (**g**), and $r > r_{\mathrm{Dirac}}$ (**h**). When the size is increased to $D$=35a, we observe that cavities become multimode mode for $r < r_{\mathrm{Dirac}}$ (**j**), remain single mode for $r = r_{\mathrm{Dirac}}$ (**k**), and become multimode again for $r > r_{\mathrm{Dirac}}$ (**l**). The Dirac singularity erases higher-order modes in open-Dirac cavities and lasers remain single-mode when the size is increased.

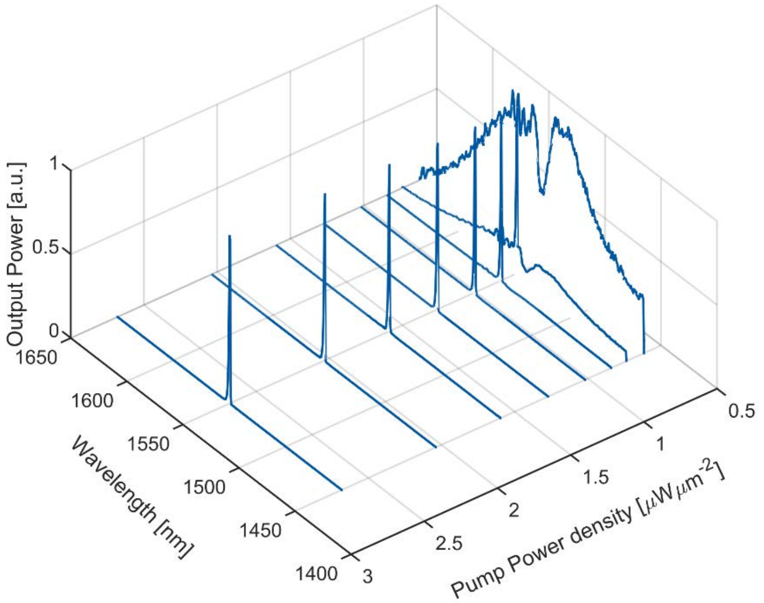

**Fig. 9.** Emission spectra from the laser ($L = 35a$). Single-mode is maintained up to $3\mu W\mu m^2$ corresponding to the power where the suspended membrane starts to be damaged.

The cavities were optically pumped at room temperature with a pulsed laser (λ = 1,064 nm, T = 12 ns pulse at a repetition rate f = 215 kHz) and the emission from each aperture was collected through a confocal microscope optimized for near-infrared spectroscopy. The photoluminescence setup is presented in Fig. 10. A 20x long working distance microscope objective (NA of 0.4) focuses the pump beam on the sample and collects the lasing emission simultaneously. The pump beam size is adjusted by a telescope (lenses $L_1$ and $L_2$) tuning the divergence of the beam. The pump power is finely tuned by an optical attenuator and monitored by a power meter. PL signals are captured by an IR-CCD and a monochromator. The spectrum is obtained in conjunction with a cooled InGaAs detector in a lock-in detection configuration.

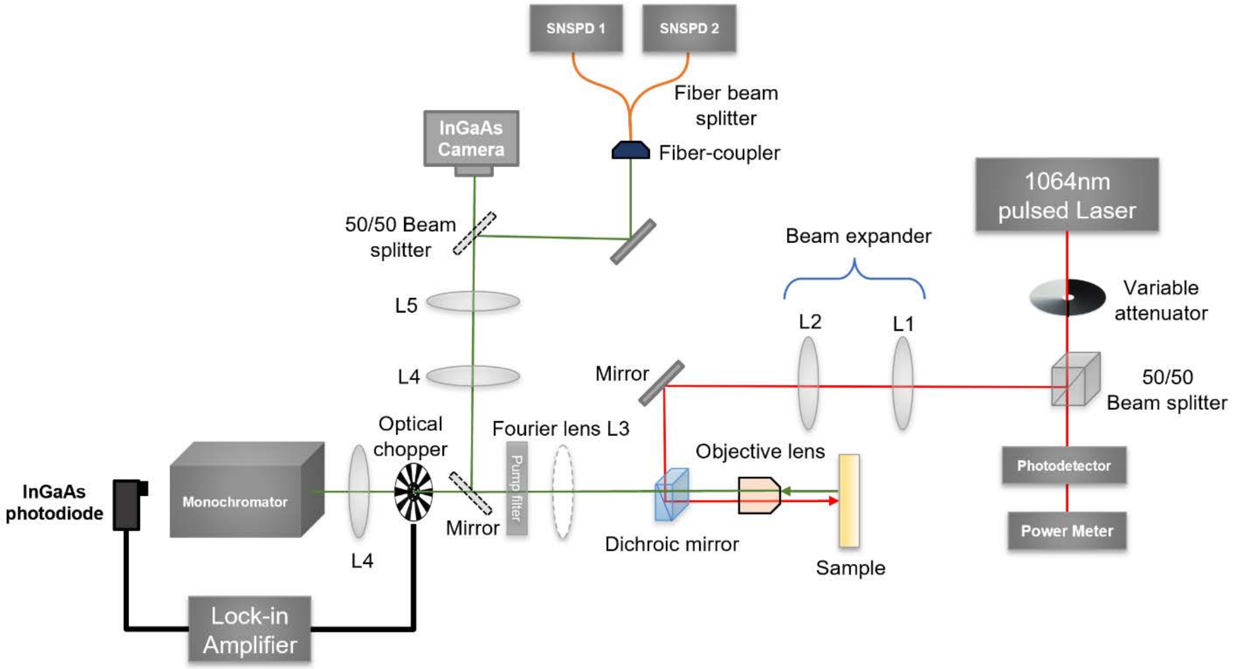

**Fig. 10.** Micro-photoluminescence for characterizing Dirac Laser. L1-L5 stands for converging lenses. SNSPD for superconducting nanowire single-photon detectors.

We have thus experimentally demonstrated the scale-invariant surface-emitting lasers that remain in single mode when the size of the cavity is increased. They are based on open-Dirac singularities and maintain single-mode lasing against size scaling. Around the open-Dirac singularity, the free spectral range is extended due to linear dispersion, while suppressing higher-order modes efficiently. These results will have implications for wave-based systems including electronics, acoustics, and photonics. The simplicity of our lasers makes them universal lasing cavities that can be used in applications including military, lidars, data communications, manufacturing as well as medical sciences and industries.

# References

1. Schawlow, A. L.,Townes, C. H. Infrared and Optical Masers. *Phys. Rev*. **112**, 1940–1949 (1958).
2. Kogelnik, H., Shank, C. V. Stimulated emission in a periodic structure. *Appl. Phys. Lett*. **18**, 152–154 (1971).
3. Soda, H., Iga, K., Kitahara, C.,Suematsu, Y. GaInAsP/InP Surface Emitting Injection Lasers. *Jpn. J. Appl. Phys*. **18**, 2329 (1979).
4. Meier, M. et al. Laser action from two-dimensional distributed feedback in photonic crystals. *Appl. Phys. Lett*. 74, 7-9 (1999).
5. Imada, M. et al. Coherent two-dimensional lasing action in surface-emitting laser with triangular-lattice photonic crystal structure. *Appl. Phys. Lett*. **75**, 316–318 (1999).
6. Choquette, K. D., Hou, H. Q., Geib, K. M. and Hammons, B. E, "Uniform and high power selectively oxidized 8x8 VCSEL array". 1997 Dig. *IEEE/LEOS Summer Topical Meetings*, Montreal, Quebec, Canada, 11–15 August 1997, pp. 11–12
7. D. Francis, H.-L. Chen, W. Yuen, G. Li, and C. Chang-Hasnain, "Monolithic 2D-VCSEL array with 2 W CW and 5 W pulsed output power," *Electron Lett*., vol. **34**, pp. 2132–2133, 1998.
8. M. Yoshida *et al.*, "Double-lattice photonic-crystal resonators enabling high-brightness semiconductor lasers with symmetric narrow-divergence beams" *Nature Materials* **18**, 121–128 (2019).
9. Hokmabadi, M. P., Nye, N. S., el-Ganainy, R., Christodoulides, D. N.,Khajavikhan, M. Supersymmetric laser arrays. *Science* **363**, 623–626 (2019).
10. X. Qiao, B. Midya, Z. Gao, Z. Zhang, H. Zhao, T. Wu, J. Yim, R. Agarwal, N. M. Litchinitser, and L. Feng, *Science* **372**, 403 (2021).
11. Novoselov, K. S. et al. Electric field effect in atomically thin carbon films. *Science* **306**, 666–669 (2004).
12. Haldane, F. D. M. Model for a quantum Hall effect without Landau levels: condensed-matter realization of the "parity anomaly". *Phys. Rev. Lett*. **61**, 2015–2018 (1988).
13. E. Yablonovitch, *Phys. Rev. Lett*. **58**, 2059–2062 (1987).
14. S. John, *Phys. Rev. Lett*. **58**, 2486–2489 (1987).
15. Sakoda, K. Universality of mode symmetries in creating photonic Dirac cones. *J. Opt. Soc. Am*. B **29**, 2770 (2012).
16. Sakoda, K. Proof of the universality of mode symmetries in creating photonic Dirac cones. *Opt. Express* 20, 25181 (2012).
17. Enoch, S., Tayeb, G., Sabouroux, P., Guérin, N.,Vincent, P. A Metamaterial for Directive Emission. *Phys. Rev. Lett*. **89**, 213902 (2002).
18. Huang, X., Lai, Y., Hang, Z. H., Zheng, H., Chan, C. T. Dirac cones induced by accidental degeneracy in photonic crystals and zero-refractive-index materials. *Nature Materials* **10**, 582–586 (2011).
19. Moitra, P. *et al.*, Realization of an all-dielectric zero-index optical metamaterial. *Nature Photonics* **7**, 791–795 (2013).
20. Li, Y. *et al.*, On-chip zero-index metamaterials. *Nature Photon*. **9**, 738–742 (2015).

21. Liberal, I.,Engheta, N. Near-zero refractive index photonics. *Nature Photon*. **11**, 149–158 (2017).
22. Jacqmin, T. *et al.* Direct observation of Dirac cones and a flatband in a honeycomb lattice for polaritons. *Phys. Rev. Lett*. **112**, 116402 (2014).
23. Bravo-Abad, J., Joannopoulos, J. D., Soljacic, M. Enabling single-mode behavior over large areas with photonic Dirac cones. *Proc. Natl Acad. Sci. USA* **109**, 9761–9765 (2012).
24. Chua, S.-L., Lu, L., Bravo-Abad, J., Joannopoulos, J. D., Soljačić, M. Larger-area single-mode photonic crystal surface-emitting lasers enabled by an accidental Dirac point. *Opt. Lett*. **39**, 2072 (2014).
25. Gao, X. et al. Dirac-vortex topological cavities. Nature Nanotechnology **15**, 1012–1018 (2020).
26. Kodigala, A. et al. Lasing action from photonic bound states in continuum. Nature 541, 196–199 (2017).
27. Loudon, R. The Quantum Theory of Light 3rd edn (Oxford Univ. Press, 2000).
28. Pan, S. H., Gu, Q., El Amili, A., Vallini, F., Fainman, Y. Dynamic hysteresis in a coherent high-β nanolaser. *Optica* **3**, 1260-1265 (2016).

# 5

# Conclusion

Thanks to the breakthrough in nanofabrication techniques in the recent decades, microcavities requiring nanoscale patternings such as subwavelength microdisk, complex waveguide cavities, and photonic crystals can be easily fabricated with unprecedently high quality. Semiconductor lasers based on microcavities offer a huge degree of freedom to modulate light waves, making themselves indispensable components in a photonic circuit and numerous applications. Achieving pure spectral coherence and single-mode operation has been always an obstacle in such microcavities. In this dissertation, different strategies to accomplish the single-mode lasing or selection of lasing mode in different types of microcavities have been presented, while these can also be generally applied to novel cavities for optical and optoelectronic applications.

In Chapter 2, it is demonstrated that through bridges, microdisks lasers can be operated under single mode with an arbitrarily selected whispering gallery mode. Due to a small modal volume and higher wave confinement, a microdisk cavity can be regarded as a zero-dimensional cavity. By protecting or breaking their fundamental $2m$-fold rotational symmetry (where $m$ is an azimuthal order) of whispering gallery mode using the bridge configuration connecting to the disk, the quality factor of modes can be controlled. We experimentally demonstrated single-mode lasing devices with specific orders of whispering gallery mode as examples.

In Chapter 3, a single-mode valley-Hall topological ring laser at telecommunication frequency has been presented. The cavity support edge mode is confined by the interface (or one-dimensional) between two inverted honeycomb lattice photonic crystals. It is shown that the degree of asymmetry in a unit cell of the photonic crystal can modulate the topological bandgap and can be used as a tuning parameter to optimize the valley-Hall cavity for single-mode lasing despite multiple cavity modes. We also identified and categorized the existing cavity modes in a valley-Hall ring cavity.

In Chapter 4, we report the first scale-invariant two-dimensional surface-emitting lasers though the size of the cavity is increased. This unconventional scaling roots from size-invariant loss term of frequency as well as the flat envelope fundamental mode. Open-Dirac singularity enables robustness against size increase by suppressing higher order modes that can compete with the fundamental target mode. We experimentally confirmed this unique scaling and believe that this result can be universally applied to the field of classical and quantum wave systems including electronics, acoustics, and photonics.